

Poisson process factorization for mutational signature analysis with genomic covariates

Alessandro Zito^{1,2}, Giovanni Parmigiani^{1,2}, and Jeffrey W. Miller¹

¹*Department of Biostatistics, Harvard T.H. Chan School of Public Health, Boston, MA, U.S.A.*

²*Department of Data Sciences, Dana Farber Cancer Institute, Boston, MA, U.S.A.*

Abstract

Mutational signatures are powerful summaries of the mutational processes altering the DNA of cancer cells. The usual approach to mutational signature analysis consists of decomposing the matrix of mutation counts from a sample of patients using non-negative matrix factorization (NMF). However, this ignores the heterogeneous patterns of mutation rates along the genome. In this paper, we introduce Poisson process factorization (PPF), which addresses this limitation by employing an inhomogeneous Poisson point process model to infer mutational signatures and their activities as they vary across the genome. PPF generalizes the baseline NMF model by representing a patient's exposure to each signature as a locus-specific function that depends on genomic covariates and patient-specific copy numbers via a log-linear model. This quantifies the relationships between genomic features and mutational signatures, and enables attribution of individual mutations to signatures. We develop tractable algorithms for *maximum a posteriori* estimation and posterior inference via Markov chain Monte Carlo. We demonstrate the method on simulated data and real data from breast cancer, using genomic covariates representing histone modifications, cell replication timing, nucleosome positioning, and DNA methylation.

Keywords: Cancer genomics; Latent factor models; Mutational signatures analysis; Non-negative matrix factorization; Poisson point processes.

1 INTRODUCTION

Cancer is associated with the accumulation of mutations in the genomes of somatic cells (Stratton et al., 2009). These mutations manifest in distinctive patterns called *mutational signatures*, which are latent vectors encoding the relative frequencies of various mutation types (Alexandrov et al., 2013). Several empirically derived signatures have been experimentally linked to biological processes such as DNA repair deficiencies, oxidative stress, or exposure to exogenous carcinogens like tobacco smoking or ultraviolet light. Detecting the activity of certain signatures in patients has led to advances in precision treatment (Aguirre et al., 2018; Samur et al., 2020), making mutational signature analysis an exciting emerging direction in cancer research (Alexandrov et al., 2020; Koh et al., 2021).

However, nearly all methods for mutational signature analysis operate at an aggregate scale, considering only the total number of each mutation type detected in the genome of each patient. This implicitly assumes a constant mutation rate across the genome, which is not generally the case; for example, see Figure 1(a). This inhomogeneity in mutation rates is well documented and relates to variation in GC content, DNA accessibility, replication timing, and epigenetic modifications, as well as copy number alterations in cancer. For example, histone modification H3K9me3 can account for nearly 40% of the variation in mutation rates at the megabase scale in many tumors (Schuster-Böckler and Lehner, 2012); see Figure 1(b) for example. Existing methods for handling this heterogeneity are either based on partitioning the genome and fitting a separate model on each region (Fischer et al., 2013), stratifying mutations according to discrete epigenetic states (Vöhringer et al., 2021), or *post hoc* association of genomic features with the estimated activity of pre-defined signatures (Otlu et al., 2023; Otlu and Alexandrov, 2025; Blokzijl et al., 2018; Lee et al., 2018, 2022; Schmalohr, 2025; Timmons et al., 2022). To our knowledge, no existing method simultaneously infers signatures and the joint effect of genomic covariates on signature activity, genome-wide.

In this article, we address this by introducing *Poisson process factorization* (PPF), a statistical framework for jointly inferring mutational signatures, their activities, and the effect of genomic covariates on such activities. Specifically, we model mutations from each signature as realizations from an inhomogeneous Poisson point process (Kingman, 1993; Daley and Vere-Jones, 2003) with a locally varying intensity function that captures the multiplicative effects of genomic covariates and copy number alterations via a log-linear model. In PPF, each signature is associated with a set of regression coefficients that quantify the enrichment or depletion of mutational burden associated with each covariate. In contrast to existing methods, these coefficients are estimated *jointly*, accounting for the effects of all covariates as well as patient-specific copy number. Furthermore, the model enables the attribution of individual mutations to signatures by providing a patient- and locus-specific probability distribution over signatures for a given mutation type.

Furthermore, PPF provides automatic selection of the number of active signatures using compressive Bayesian hyperpriors (Zito and Miller, 2024), which avoids computationally intensive rank selection procedures by shrinking the activities of redundant signatures to negligible values. We develop a computationally efficient algorithm for *maximum a posteriori* estimation using majorization-minimization (Lee and Seung, 2000) coupled with Newton’s method, and present a Markov chain Monte Carlo sampler for fully Bayesian inference.

The article is structured as follows. Section 2 provides background on mutational signature analysis, then introduces the Poisson process factorization (PPF) model. Section 3 presents algorithms for estimation and

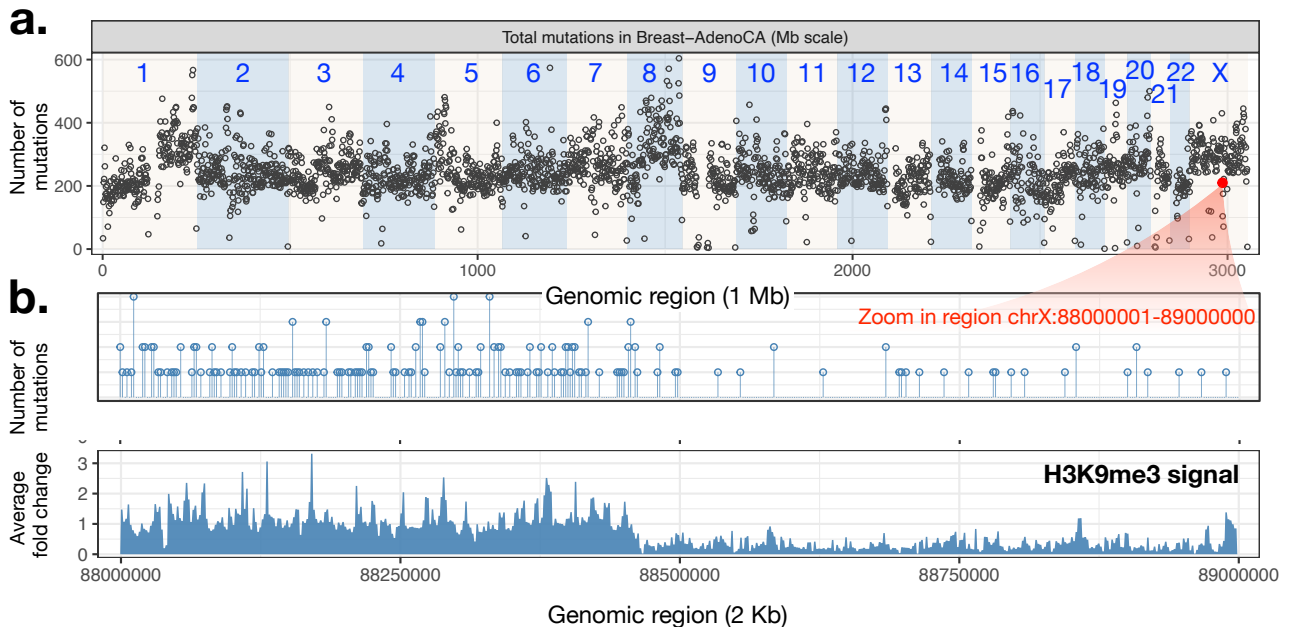


Figure 1: (a) Number of single-base substitutions in 1-megabase bins in 113 breast adenocarcinomas from the International Cancer Genome Consortium (ICGC). Alternating colored bands and numbers indicate chromosomes. (b) Top: Number of mutations in 2-kilobase bins for region chrX:88,000,001-89,000,000, highlighted by the red point. Bottom: Average signal (fold-change with respect to assay background) in the same bins for histone modification H3K9me3, in breast epithelium tissue; see Supplementary material.

inference in PPF. Section 4 conducts a simulation study, and Section 5 contains an application to data from an ICGC cohort of 113 breast cancer patients. Future directions are discussed in Section 6.

2 MODEL

In this section, we provide background on mutational signature analysis (Section 2.1), introduce the PPF model (Section 2.2), describe the log-linear parametrization for the effect of genomic covariates (Section 2.3), and specify our prior distributions (Section 2.4).

2.1 BACKGROUND ON MUTATIONAL SIGNATURE ANALYSIS

Since DNA has a double-stranded structure where nucleotide A always binds with T, and C always binds with G, six distinct substitutions can happen at any genomic position: $C>A$, $C>T$, $C>G$, $T>A$, $T>C$, or $T>G$, where $C>A$ denotes a mutation from the pair C:G into the pair A:T. Moreover, it has been observed that mutation rates depend strongly on the adjacent bases (Nik-Zainal et al., 2012). Hence, it is common practice to further categorize single-base substitutions (SBS) according to the trinucleotide context, leading to a total of $I = 4 \times 6 \times 4 = 96$ mutation types, sometimes called channels (Alexandrov et al., 2013). For instance, $T[C>A]G$ indicates a $C>A$ mutation where T and G are the nucleotides flanking C on the 5' and 3' sides, respectively.

Let $N_{ij} \in \mathbb{N} = \{0, 1, 2, \dots\}$ be the number of mutations of type $i = 1, \dots, I$, $I = 96$, for patient $j = 1, \dots, J$, and let $N \in \mathbb{N}^{I \times J}$ denote the matrix with entries N_{ij} . The standard approach to mutational signature analysis uses non-negative matrix factorization (NMF; Lee and Seung, 1999) to approximate N by the product $R\Theta$,

where $R \in \mathbb{R}_+^{I \times K}$ is the *mutational signature* matrix, and $\Theta \in \mathbb{R}_+^{K \times J}$ is the *activity* matrix. Here, $K \geq 1$ is the rank of the factorization and represents the number of active mutational processes. In traditional NMF, R and Θ are estimated by minimizing a loss function such as the squared Euclidean distance or the Kullback–Leibler divergence; see Gillis (2020).

From a probabilistic modeling perspective, it is common to assume

$$N_{ij} \sim \text{Poisson} \left(\sum_{k=1}^K r_{ik} \theta_{kj} \right) \quad (1)$$

independently for each i and j , where $\text{Poisson}(\lambda)$ denotes the Poisson distribution with mean λ . Here, $r_k = (r_{1k}, \dots, r_{Ik})$ and $\theta_k = (\theta_{k1}, \dots, \theta_{kJ})$ are the k th column of R and the k th row of Θ , respectively. With the constraint $\sum_{i=1}^I r_{ik} = 1$, the vector r_k represents the relative frequencies with which each of the 96 mutation types are generated by signature k , and θ_{kj} represents its activity in patient j . See Zhou and Carin (2015) for an overview.

2.2 POISSON PROCESS FACTORIZATION

A point process is a stochastic model for the locations of randomly placed points, which we interpret as mutations. Let $T \geq 0$ be the length of the reference genome and let $A \subseteq [0, T)$ represent a region of the genome. To simplify tractability, we assume that $[0, T)$ is a continuous approximation of the genome where any arbitrarily defined region A is Borel measurable. Such approximation is reasonable, since in practice $T \approx 3 \times 10^9$ in our application. A *Poisson point process* with intensity function $\lambda_{ij} : [0, T) \rightarrow \mathbb{R}_+$ is a counting process Z_{ij} such that (i) $Z_{ij}(A) \sim \text{Poisson}(\int_A \lambda_{ij}(t) dt)$ for all regions $A \subseteq [0, T)$, and (ii) $Z_{ij}(A_1), \dots, Z_{ij}(A_m)$ are independent for all pairwise disjoint regions $A_1, \dots, A_m \subseteq [0, T)$. Note that the intensity determines the expected number of points in A , since $\mathbb{E}(Z_{ij}(A)) = \int_A \lambda_{ij}(t) dt$. If $\lambda_{ij}(t)$ takes the same value for all t , then the process is called *homogeneous*; otherwise, the process is *inhomogeneous* (Kingman, 1993).

We model the mutations as following inhomogeneous Poisson point processes Z_{ij} , independently for all i and j , where $Z_{ij}(A)$ denotes the number of mutations of type i observed in region A for patient j . An attractive feature of Poisson point processes is that the likelihood takes a relatively simple form. Suppose that for a given i and j , we observe N_{ij} mutations at positions $t_{ij1}, \dots, t_{ijN_{ij}}$, where $t_{ijn} \in [0, T)$ for each $n = 1, \dots, N_{ij}$. It can be shown (Daley and Vere-Jones, 2003, Chapter 2) that the likelihood of the intensity functions $\lambda = (\lambda_{ij})$ is

$$\mathcal{L}(\lambda) = \prod_{i=1}^I \prod_{j=1}^J \exp \left(- \int_0^T \lambda_{ij}(t) dt \right) \prod_{n=1}^{N_{ij}} \lambda_{ij}(t_{ijn}). \quad (2)$$

The flexibility of the specification arising from Equation (2) lies in the choice of the functional form of the intensity λ_{ij} . Mirroring Equation (1), we let

$$\lambda_{ij}(t) = \sum_{k=1}^K r_{ik} \vartheta_{kj}(t), \quad t \in [0, T), \quad (3)$$

for each mutation type $i = 1, \dots, I$ and patient $j = 1, \dots, J$. As before, K is the rank of the factorization and $r_k = (r_{1k}, \dots, r_{Ik})$ is the k th mutational signature, but now $\vartheta_{kj} : [0, T] \rightarrow \mathbb{R}_+$ is a position-dependent *activity function* that quantifies the rate of mutations due to signature k at locus t in patient j .

We refer to the model specified by Equations (2) and (3) as *Poisson process factorization* (PPF). The following proposition shows that the standard Poisson NMF model in Equation (1) occurs as a special case when all activity functions are constant.

Proposition 1. *Consider a collection of inhomogeneous Poisson point processes Z_{ij} on $[0, T]$ with intensity functions λ_{ij} as in Equation (3). If $\vartheta_{kj}(t) = \theta_{kj}/T$ for all $t \in [0, T]$ and all i, j, k , then inference for r_{ik} and θ_{kj} is equivalent under Equation (2) and Equation (1).*

As a result, PPF can be viewed as a flexible generalization of NMF that allows the activities to depend on position t . For a related generalization in the context of user-item recommendations, see [Hosseini et al. \(2020\)](#). Our approach differs from previous approaches for point processes with a factorized intensity function ([Miller et al., 2014](#); [Lloyd et al., 2016](#); [Hosseini et al., 2020](#)), which are primarily designed to capture either spatial or temporal autoregressive trends in the data rather than covariate-driven effects.

Similar to Poisson NMF ([Lee and Seung, 1999](#)), the PPF model can be decomposed into a sum of K independent processes, each representing the activity of a distinct mutational signature. This is a consequence of the superposition theorem ([Kingman, 1993](#)).

Proposition 2. *Let Y_{ij1}, \dots, Y_{ijK} be independent, inhomogeneous Poisson point processes on $[0, T]$ such that Y_{ijk} has intensity function $\lambda_{ijk}(t) = r_{ik}\phi_{kj}(t)$ for $t \in [0, T]$. Then $\sum_{k=1}^K Y_{ijk}$ is a Poisson point process with the intensity function in Equation (3).*

2.3 LOG-LINEAR MODEL FOR EFFECT OF GENOMIC COVARIATES

In Equation (3), the activities are allowed to vary with the genomic position t , whereas the signatures are constant in t . Holding the signatures constant allows us to interpret variations in the mutation rate as variations in the activity of specific signatures. Moreover, it facilitates comparisons of the inferred signatures with the reference signatures in the *Catalogue of Somatic Mutations in Cancer* (COSMIC; [Tate et al., 2018](#)), helping to clarify the underlying biological processes. This is because COSMIC provides a curated collection of signatures and their etiology across multiple tumors and environmental agents.

To parametrize the activity functions $\vartheta_{kj}(t)$, we propose a log-linear model that leverages genomic covariates as well as patient-specific factors. Suppose there are L known covariate functions $x_\ell : [0, T] \rightarrow \mathbb{R}$ for $\ell = 1, \dots, L$, with $x_\ell(t)$ denoting the value of covariate ℓ at position t . Denote their vector representation by $\mathbf{x}(t) = (x_1(t), \dots, x_L(t)) \in \mathbb{R}^L$. For example, $x_\ell(t)$ may be the intensity of the signal indicating a histone modification such as H3K36me3, H3K27ac, or H3K9me3, as in Figure 1. Additionally, let $c_j : [0, T] \rightarrow \mathbb{R}_+$ be a non-negative function such that $c_j(t)$ is the copy number at position t in patient j . Both $\mathbf{x}(t)$ and $c_j(t)$ are assumed to be fixed and known based on other data. Note that $\mathbf{x}(t)$ is shared across all patients, whereas $c_j(t)$ is patient-specific.

We model the activity functions in Equation (3) as

$$\vartheta_{kj}(t) = \frac{1}{2} \phi_{kj} c_j(t) e^{\beta_k^\top \mathbf{x}(t)}, \quad t \in [0, T], \quad (4)$$

where $\phi_{kj} > 0$ for each k, j , and $\boldsymbol{\beta}_k = (\beta_{k1}, \dots, \beta_{kL}) \in \mathbb{R}^L$ for each k . Here, ϕ_{kj} is the baseline activity of signature k in patient j , while, $\boldsymbol{\beta}_k$ is a vector of regression coefficients capturing the effect of $\mathbf{x}(t)$ on the rate of mutations due to signature k at position t . The copy number $c_j(t) \geq 0$ affects the mutation rate at location t in patient j , irrespective of the signature. In a normal genome, $c_j(t) = 2$ since there are two copies of each chromosome, except for X and Y in males. Thus, the factor $c_j(t)/2$ is the ratio of observed to expected copy number. The baseline function $\vartheta_{kj}(t) = \phi_{kj}$ is a special case occurring when $c_j(t) = 2$ and $\boldsymbol{\beta}_k^\top \mathbf{x}(t) = 0$ for all t . This is the case described by Proposition 1, where $\phi_{kj} = \theta_{kj}/T$ and activities are constant.

Importantly, the effects of genomic covariates are modeled as *multiplicative* in Equation (4). This makes it possible to capture effects that suppress mutational activity as well as those that amplify it. Specifically, a one-unit increase or decrease in $x_\ell(t)$ implies an $|e^{\beta_{k\ell}} - 1|$ percent increase or decrease, respectively, in the activity of signature k at t .

The expected number of mutations of type i in region A for patient j is

$$\mathbb{E}(Z_{ij}(A) \mid R, \Phi, B) = \sum_{k=1}^K r_{ik} \phi_{kj} \int_A \frac{1}{2} c_j(t) e^{\boldsymbol{\beta}_k^\top \mathbf{x}(t)} dt, \quad (5)$$

where $R = (r_{ik}) \in \mathbb{R}^{I \times K}$, $\Phi = (\phi_{kj}) \in \mathbb{R}^{K \times J}$ and $B = (\beta_{k\ell}) \in \mathbb{R}^{K \times L}$ denote the matrices of signatures, activities, and regression coefficients, respectively. Given R , Φ , and B , the integral in Equation (5) can be calculated via binning, considering that metrics used to represent genomic features are typically stepwise constant; see Section 5.

Previous approaches that employ covariates in inhomogeneous Poisson process differ from Equation (4) in that they use fixed covariates \mathbf{x} rather than position-dependent covariates $\mathbf{x}(t)$ (Lawless, 1987). Specifically, these approaches use the intensity function $\lambda(t) = \lambda_0(t) e^{\boldsymbol{\beta}^\top \mathbf{x}}$, where $\lambda_0(t)$ is a baseline that is often modeled nonparametrically.

2.4 PRIOR DISTRIBUTIONS

Our prior construction extends the hierarchical model of Zito and Miller (2024), employing *compressive hyperpriors* to provide automatic selection of the number of latent factors. Specifically, for each $k = 1, \dots, K$, we take

$$r_k = (r_{1k}, \dots, r_{Ik}) \sim \text{Dir}(\alpha_{1k}, \dots, \alpha_{Ik}), \quad (6)$$

$$\phi_{k1}, \dots, \phi_{kJ} \mid \mu_k \sim \text{Ga}\left(a, \frac{a}{\mu_k} \int_0^T \frac{1}{2} c_j(t) dt\right), \quad (7)$$

$$\mu_k \sim \text{InvGa}(aJ + 1, \varepsilon aJ), \quad (8)$$

$$\boldsymbol{\beta}_k \mid \sigma_k^2 \sim \text{N}(\mathbf{0}, \sigma_k^2 I_L), \quad \sigma_k^2 \sim \text{InvGa}(c_0, d_0), \quad (9)$$

where $a, \varepsilon, c_0, d_0 > 0$, $\text{Dir}(\alpha_1, \dots, \alpha_J)$ is a Dirichlet distribution, $\text{Ga}(a, b)$ is a gamma distribution with mean a/b , $\text{InvGa}(a_0, b_0)$ is an inverse gamma with mean $b_0/(a_0 - 1)$ for $a_0 > 1$, $\text{N}(\mathbf{m}, \boldsymbol{\Sigma})$ is the multivariate normal distribution with mean $\mathbf{m} \in \mathbb{R}^L$ and positive definite covariance matrix $\boldsymbol{\Sigma} \in \mathbb{R}^{L \times L}$, and I_L is the $L \times L$ identity matrix. As defaults, we set $a = 1.01$, $\varepsilon = 0.001$, $c_0 = 100$, $d_0 = 1$, and $\alpha_{ik} = 1.01$.

This choice of prior has several important features. Using a Dirichlet prior in Equation (6) avoids the scaling ambiguities that arise in NMF, since it constrains $\sum_{i=1}^I r_{ik} = 1$. The prior on baseline activity ϕ_{kj} in Equation (7) ensures $\mu_k = \mathbb{E}(\phi_{kj} | \mu_k) \int_0^T \frac{1}{2} c_j(t) dt$, so that μ_k controls the total baseline contribution of signature k over the whole genome, accounting for copy number. Each hyperparameter μ_k , referred to as the *relevance weight* for signature k , is given the data-dependent *compressive hyperprior* in Equation (8), which favors small values of μ_k since $\mathbb{E}(\mu_k) = \varepsilon$ *a priori*. Consequently, when signature k is not needed, the posteriors on μ_k and $\phi_{k1}, \dots, \phi_{kJ}$ concentrate near ε , effectively removing it from the decomposition; see Zito and Miller (2024). Finally, the coefficients β_k and variance σ_k^2 follow a normal-inverse gamma prior, which facilitates posterior computation. The default settings of $c_0 = 100$ and $d_0 = 1$ make β_k concentrated near zero *a priori*, encouraging sparsity. Meanwhile, $\beta_{k\ell}$ moves away from zero when covariate ℓ can help explain position-specific variations in mutation rate for signature k .

3 ALGORITHMS FOR POISSON PROCESS FACTORIZATION

In this section, we present a MAP point estimation algorithm (Section 3.1) and a Markov chain Monte Carlo algorithm for fully Bayesian inference (Section 3.2).

3.1 MAXIMUM A POSTERIORI (MAP) ESTIMATION

We first derive a majorization-minimization algorithm to compute a *maximum a posteriori* estimate of the PPF model parameters, inspired by the algorithm of Lee and Seung (2000) for NMF. In simple terms, a majorizer for $f(x)$ is a function $g(y, x)$ of two arguments such that (i) $g(y, x) \geq f(y)$ for all y , and (ii) $g(x, x) = f(x)$ for all x . As a result, if $y = \arg \min_z g(z, x)$, then $f(x) = g(x, x) \geq g(y, x) \geq f(y)$. Hence, minimizing g implicitly minimizes f as well, which is advantageous when the minima of the majorizer are analytically simple to compute, compared to minimizing the original function. In our model, the target f is the negative log posterior density

$$\begin{aligned}
 -\log \pi(R, \Phi, B, \mu, \sigma^2 | \mathbf{t}) = & \\
 = \sum_{jk} \phi_{kj} \int_0^T \frac{1}{2} c_j(t) e^{\beta_k^\top \mathbf{x}(t)} dt - \sum_{ij} \sum_{n=1}^{N_{ij}} \log \left(\sum_{k=1}^K r_{ik} \phi_{kj} \frac{1}{2} c_j(t_{ijn}) e^{\beta_k^\top \mathbf{x}(t_{ijn})} \right) & \quad (10) \\
 - \log \pi(R) \pi(\Phi | \mu) \pi(\mu) \pi(B | \sigma^2) \pi(\sigma^2) + \text{const}, &
 \end{aligned}$$

subject to the constraints that r_{ik} , ϕ_{kj} , μ_k , and σ_k^2 are positive and $\sum_{i=1}^I r_{ik} = 1$ for all k . In Equation (10), the bottom line represents the priors from Section 2.4 and $\mathbf{t} = (t_{ijn})$ denotes the collection of observed mutation positions for all i, j , and $n = 1, \dots, N_{ij}$.

Algorithm 1 presents the steps for one iteration of our method for minimizing Equation (10). A complete derivation is in Section S3. Steps 1 and 2 update the signatures and baseline activities in a multiplicative manner, ensuring that the positivity requirements are automatically satisfied, provided that $a \geq 1$ and $\alpha_{ik} \geq 1$. Step 3 updates β_k by majorizing Equation (10) with respect to β_k and then applying Newton’s method using the gradient \mathbf{g}_k and the Hessian matrix \mathbf{H}_k of the majorizer with respect to β_k . Step 4 updates μ_k and σ_k^2 by minimizing their full conditional densities, which have a closed form solution.

Algorithm 1. MAP updates for Poisson process factorization

1 **Signatures:** for $k = 1, \dots, K$ do

Update each probability r_{ik} for $i = 1, \dots, I$ in signature k as

$$r'_{ik} \leftarrow \alpha_{ik} - 1 + \sum_j \sum_{n=1}^{N_{ij}} \frac{r_{ik} \phi_{kj} e^{\beta_k^\top \mathbf{x}(t_{ijn})}}{\sum_{s=1}^K r_{is} \phi_{sj} e^{\beta_s^\top \mathbf{x}(t_{ijn})}}, \quad r_{ik} \leftarrow \frac{r'_{ik}}{\sum_i r'_{ik}}.$$

2 **Baseline activities:** for $j = 1, \dots, J$ and $k = 1, \dots, K$ do

Update each ϕ_{kj} as

$$\phi_{kj} \leftarrow \left(a - 1 + \sum_i \sum_{n=1}^{N_{ij}} \frac{r_{ik} \phi_{kj} e^{\beta_k^\top \mathbf{x}(t_{ijn})}}{\sum_{s=1}^K r_{is} \phi_{sj} e^{\beta_s^\top \mathbf{x}(t_{ijn})}} \right) \left(\int_0^T \frac{1}{2} c_j(t) (e^{\beta_k^\top \mathbf{x}(t)} + a/\mu_k) dt \right)^{-1},$$

3 **Regression coefficients:** for $k = 1, \dots, K$ do

Update the regression coefficients with Newton's method as $\beta_k \leftarrow \beta_k - \mathbf{H}_k^{-1} \mathbf{g}_k$, where

$$\mathbf{H}_k = \sum_j \phi_{kj} \int_0^T \frac{1}{2} c_j(t) e^{\beta_k^\top \mathbf{x}(t)} \mathbf{x}(t) \mathbf{x}(t)^\top dt + \frac{1}{\sigma_k^2} I_L$$

$$\mathbf{g}_k = \sum_j \phi_{kj} \int_0^T \frac{1}{2} c_j(t) e^{\beta_k^\top \mathbf{x}(t)} \mathbf{x}(t) dt - \sum_{ij} \sum_{n=1}^{N_{ij}} \frac{r_{ik} \phi_{kj} e^{\beta_k^\top \mathbf{x}(t_{ijn})}}{\sum_{s=1}^K r_{is} \phi_{sj} e^{\beta_s^\top \mathbf{x}(t_{ijn})}} \mathbf{x}(t_{ijn}) + \frac{1}{\sigma_k^2} \beta_k.$$

4 **Relevance weights and variance parameters:** for $k = 1, \dots, K$ do

Update each parameter as μ_k as

$$\mu_k \leftarrow \frac{\varepsilon a J + a \sum_j \phi_{kj} \int_0^T \frac{1}{2} c_j(t) dt}{2aJ + 2}, \quad \sigma_k^2 \leftarrow \frac{d_0 + \beta_k^\top \beta_k / 2}{c_0 + L/2 + 1}.$$

Output: Updated point estimates for $R, \Phi, B, \mu, \sigma^2$.

We cycle through Steps 1–4 of Algorithm 1 until the relative difference between two successive evaluations of Equation (10) (excluding the constant) is lower than a tolerance, set at 10^{-7} by default. To improve convergence, we repeat Step 3 two times each cycle. To improve numerical stability, we find it beneficial to modify Step 3 to cap the root-mean-square of the update at a fixed value $\rho > 0$ by using $\beta_k \leftarrow \beta_k + \xi_k \min \{1, \rho \sqrt{L} / \|\xi_k\|\}$ where $\xi_k = -\mathbf{H}_k^{-1} \mathbf{g}_k$ and $\|\cdot\|$ is the Euclidean norm, following [Miller and Carter \(2020\)](#); we find $\rho = 0.5$ works well in practice.

3.2 POSTERIOR INFERENCE WITH MARKOV CHAIN MONTE CARLO

The optimization approach in Section 3.1 is a computationally efficient way of obtaining point estimates for PPF. However, it is often important to quantify uncertainty in the parameters, especially when assessing the effects of the covariates.

In Algorithm 2, we provide a Markov chain Monte Carlo (MCMC) sampler for the PPF posterior. To facilitate posterior sampling, we use the following data augmentation technique in which we introduce a multinomial random variable for each observed mutation. Specifically, for the n th mutation of type i in patient j , we let

Algorithm 2. MCMC sampler updates for Poisson process factorization

1 Latent attributions: for $i = 1, \dots, I$ and $j = 1, \dots, J$ and $n = 1, \dots, N_{ij}$ do

Update the latent attribution for the mutation at position t_{ijn} by drawing

$$W_{ij}(t_{ijn}) \sim \text{Mult}(1; p_{ij1}(t_{ijn}), \dots, p_{ijK}(t_{ijn})), \quad p_{ijk}(t_{ijn}) = \frac{r_{ik}\phi_{kj}e^{\beta_k^\top \mathbf{x}(t_{ijn})}}{\sum_{s=1}^K r_{is}\phi_{sj}e^{\beta_s^\top \mathbf{x}(t_{ijn})}}.$$

2 Signatures: for $k = 1, \dots, K$ do

Define $M_{ik} = \sum_j \sum_{n=1}^{N_{ij}} W_{ijk}(t_{ijn})$ and update r_k by drawing

$$r_k \sim \text{Dir}(\alpha_{1k} + M_{1k}, \dots, \alpha_{Ik} + M_{Ik}).$$

3 Baseline activities: for $j = 1, \dots, J$ and $k = 1, \dots, K$ do

Define $S_{kj} = \sum_i \sum_{n=1}^{N_{ij}} W_{ijk}(t_{ijn})$ and update ϕ_{kj} by drawing

$$\phi_{kj} \sim \text{Ga}\left(a + S_{kj}, \int_0^T \frac{1}{2} c_j(t) \left(\frac{a}{\mu_k} + e^{\beta_k^\top \mathbf{x}(t)}\right) dt\right).$$

4 Regression coefficients: for $k = 1, \dots, K$ do

Update β_k using elliptical slice sampling (Murray et al., 2010) with target density

$$f(\beta_k) \propto \exp\left(-\sum_j \phi_{kj} \int_0^T \frac{1}{2} c_j(t) e^{\beta_k^\top \mathbf{x}(t)} dt + \sum_{ij} \sum_{n=1}^{N_{ij}} W_{ijk}(t_{ijn}) \beta_k^\top \mathbf{x}(t_{ijn})\right) \text{N}(\beta_k; 0, \sigma_k^2 I_L).$$

5 Relevance weights and variances: for $k = 1, \dots, K$ do

Update μ_k and σ_k^2 by drawing

$$\begin{aligned} \mu_k &\sim \text{InvGa}\left(2aJ + 1, \varepsilon aJ + a \sum_j \phi_{kj} \int_0^T \frac{1}{2} c_j(t) dt\right), \\ \sigma_k^2 &\sim \text{InvGa}(c_0 + L/2, d_0 + \beta_k^\top \beta_k/2). \end{aligned}$$

Output: Updated sample from the joint posterior of R, Φ, B, μ , and σ^2 .

$W_{ij}(t_{ijn}) = (W_{ij1}(t_{ijn}), \dots, W_{ijK}(t_{ijn})) \sim \text{Mult}(1; p_{ij1}(t_{ijn}), \dots, p_{ijK}(t_{ijn}))$ given R, Φ, B , and \mathbf{t} , where

$$p_{ijk}(t_{ijn}) = \mathbb{P}(W_{ijk}(t_{ijn}) = 1 \mid R, \Phi, B, \mathbf{t}) = \frac{r_{ik}\phi_{kj}e^{\beta_k^\top \mathbf{x}(t_{ijn})}}{\sum_{s=1}^K r_{is}\phi_{sj}e^{\beta_s^\top \mathbf{x}(t_{ijn})}}. \quad (11)$$

Then, conditionally on all of these multinomial random variables, denoted W collectively, we obtain conjugate updates for the signatures, the baseline activities, and the relevance weights (Steps 2, 3, and 5, respectively, in Algorithm 2). The full conditional distribution for the regression coefficients does not take a form that can be sampled from directly, however, we can use elliptical slice sampling (Murray et al., 2010) thanks to the Gaussian prior over β_k ; see Step 4. Although evaluations of the target are expensive due to the large dimension of the genome, this method is practical since it does not require any tuning.

In Equation (11), $p_{ijk}(t_{ijn})$ represents the probability that the mutation of type i in patient j at position t_{ijn} is due to signature k . Unlike the multinomial data augmentation in Bayesian Poisson NMF (Zhou and Carin, 2015), these probabilities are not constant, but vary along the genome depending on values of the covariates. This novel aspect of PPF can provide valuable insight since mutations of type i may be attributed to one signature at some locations, and another signature elsewhere.

4 SIMULATIONS

4.1 SETUP

We generate synthetic data to evaluate the performance of the PPF model and our algorithms under different scenarios and settings.

Data simulation. We simulate data for $J = 40$ patients, with $L = 10$ covariates and $K_0 = 8$ signatures (4 from COSMIC, 4 random). We use only the first $L_{\text{true}} = 5$ covariates to generate the mutations, setting $\beta_{k\ell} = 0$ for $\ell = 6, \dots, 10$, so that the last 5 covariates do not affect the mutation rate. We consider two cases: in Scenario A, the covariates are independent, while in Scenario B, they reflect the strong correlations exhibited by certain genomic features, as illustrated in Figure S2. Under each scenario, we generate 20 datasets—each with its own covariates, copy numbers, true parameters, and mutations—resulting in an average total number of mutations across replicates equal to 94,577 and 92,860 in Scenarios A and B, respectively. See Section S4 for full details on how the datasets are simulated.

Methods compared. On each simulated dataset, we compare results from the following methods:

- (i) MAP, true \mathbf{x} – the MAP with only the $L = 5$ covariates used to generate the data.
- (ii) MAP, all \mathbf{x} – the MAP with all $L = 10$ covariates.
- (iii) MCMC, all \mathbf{x} – the posterior mean for the same model in (ii).
- (iv) MAP, CompNMF – the MAP of Equation (1) with priors as in [Zito and Miller \(2024\)](#).

The PPF models in (i), (ii), and (iii) all use the true copy numbers $c_j(t)$. We set $a = 1.01$, $\alpha_{ik} = 1.01$, $\varepsilon = 0.001$, $c_0 = 100$, $d_0 = 1$, and $K = 15$. Additional comparisons against versions using copy numbers only, with no other covariates, and coarser aggregations for the simulated covariates are reported in the Supplementary material (Section S4).

Computation. For methods (i) and (ii), we run Algorithm 1 until the relative difference in log-posterior is less than 10^{-7} . For method (iv), we use the multiplicative rules in Algorithm S1 with tolerance 10^{-7} . For the MAP algorithms, we initialize by randomly drawing from the priors. For method (iii), we initialize by using Algorithm 1 to estimate the MAP, and then use it as a starting point for Algorithm 2, running one MCMC chain for 3,000 iterations and discarding the first 1,500 as burn-in. Let \hat{R} , $\hat{\Phi}$, \hat{B} , $\hat{\mu}$, and $\hat{\sigma}^2$ denote the parameter estimates, specifically, these are the posterior modes when using Algorithm 1 and the posterior means when using Algorithm 2.

Postprocessing. We postprocess the output to eliminate redundant factors using the thresholding rule of [Zito and Miller \(2024\)](#), as follows. We discard all signatures for which $\hat{\mu}_k \leq 5\varepsilon$ and the cosine similarity between \hat{r}_k and the uniform vector $(1/96, \dots, 1/96)$ exceeds 0.975. Thus, a latent process is excluded from the factorization when its average activity is close to $\varepsilon = 0.001$ and the associated signature is nearly constant. The number of signatures remaining is an estimate of the rank, \hat{K} .

For each dataset, we calculate $\text{RMSE}(\hat{R}, R_0)$, $\text{RMSE}(\hat{\Theta}, \Theta_0)$, and $\text{RMSE}(\hat{B}, B_0)$, where $\text{RMSE}(\hat{A}, A) = (\sum_{ij} (\hat{a}_{ij} - a_{ij})^2 / mn)^{1/2}$ denotes the root mean-squared error between two matrices of dimension $m \times n$. Here, $\Theta_0 \in \mathbb{R}^{K \times J}$ is the matrix with entry (k, j) equal to $\int_0^T \vartheta_{kj}^0(t) dt$, where $\vartheta_{kj}^0(t)$ is defined as in Equation (4) but using the true parameter values; likewise, $\hat{\Theta}$ is defined similarly but using the estimated parameter values. These quantities represent the total activity of each signature across the genome. We assess these integrated

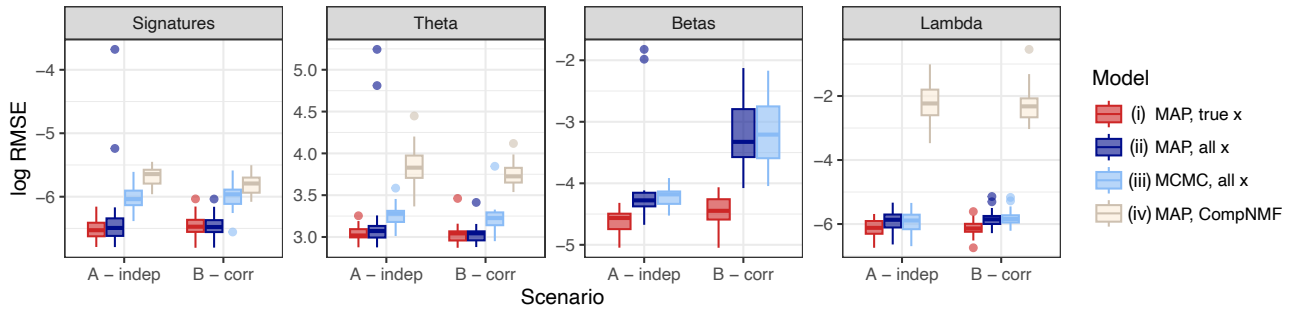


Figure 2: Results of the simulation described in Section 4.1 in terms of $\log(\text{RMSE})$ for the parameters of the simulation. Boxplots display the values from 20 randomly generated datasets under both scenarios. The panels display the $\log(\text{RMSE})$ of (\hat{R}, R_0) , $(\hat{\Theta}, \Theta_0)$, (\hat{B}, B_0) , and $(\hat{\Lambda}, \Lambda_0)$.

activities rather than the baseline activities because they have a consistent meaning across both PPF and NMF. To calculate the RMSE, we first complete all matrices with zeros to avoid any potential misalignment between \hat{K} and the relevant true value. Then, we match estimated signatures—along with the corresponding activities and regression coefficients—to the true signatures using the Hungarian algorithm with cosine similarity.

4.2 SIMULATION RESULTS

Estimation of the number of signatures. All four methods correctly return $\hat{K} = 8$ on every dataset in both scenarios, except for method (ii) on one dataset in Scenario A; see Figure S1. Moreover, the signatures are retrieved with precision and sensitivity near one; see the values of the F_1 score in Figure S1.

Parameter estimation. Figure 2 shows the estimation performance of each method in terms of recovering the data-generating parameters, plotted on the log scale to facilitate visualization. First, note that the RMSEs for R_0 and Θ_0 are considerably better when covariates are included: compare methods (i)-(iii) to (iv). Hence, even though the baseline NMF retrieves the correct number of signatures in every case with high precision, accounting for covariates and copy numbers improves inference for R_0 and Θ_0 .

The best performance is achieved by the MAP when the model is correctly specified, that is, method (i), with $L = L_{\text{true}} = 5$. The inclusion of redundant covariates in method (ii) does not strongly impact the retrieval of R_0 and Θ_0 in either scenario, except for the two outliers in Scenario A in which $\hat{K} = 9$. Interestingly, the posterior mean from method (iii) performs somewhat worse when estimating R_0 and Θ_0 , even though the MCMC chain was started at the solution from (ii). While we do not observe a difference when estimating the regression coefficients B_0 . When estimating B_0 , the correlated covariates in Scenario B lead to an appreciable loss in performance in models (ii) and (iii) compared to (i).

Intensity function estimation. In the fourth panel of Figure 2, we evaluate how well each method estimates the average intensity function by calculating $\text{RMSE}(\hat{\Lambda}, \Lambda_0) = (\sum_m (\hat{\Lambda}_{jm} - \Lambda_{jm})^2 / JM)^{1/2}$ for each dataset, where $\Lambda_{jm} = \sum_i \int_{\tau_m}^{\tau_{m+1}} \lambda_{ij}(t) dt$ is the total intensity in bin m , and $\hat{\Lambda}_{jm}$ is its estimated value. Method (iv), which does not incorporate covariates, has again the worst performance. The RMSEs for models (ii) and (iii) are virtually identical. This suggests that the posterior mean’s worse performance than the MAP when estimating signatures and activities does not strongly affect the performance when estimating mutation rates.

5 APPLICATION: ICGC BREAST ADENOCARCINOMA

We analyze whole-genome sequencing data from 113 women with breast cancer from the **Breast-AdenoCA** ICGC cohort of [The ICGC/TCGA Pan-Cancer Analysis of Whole Genomes Consortium \(2020\)](#). The data consist of 707,104 mutations in total, for which we have access to the genomic position (e.g., `chrX:77364730-77364827`) and the single-base substitution with trinucleotide context (e.g., `A[C>T]C`). The patients’ mutational data are variable: the median number of mutations per patient is 4,125, and there are four hypermutated patients with more than 20,000 mutations each, the largest of which has 64,464 mutations (patient DO1076).

We also have access to estimated copy numbers $c_j(t)$, genome-wide, for each patient in the cohort. In some regions, the estimated copy number is missing (on average, for $< 1.5\%$ of the genome); in such cases, we impute the missing values as $c_j(t) = 2$, representing the normal condition. Importantly, variations in copy number are correlated with the mutation rate at the Mb scale ($\rho = 0.44$, $p < 2.2 \times 10^{-16}$). For example, the average copy numbers in chromosome arms 1p and 1q are 2.42 and 3.90, respectively, with associated average mutation counts equal to 217 and 304, across all patients. This explains the jump in mutation rate in the middle of chromosome 1 in Figure 1.

We use covariates for histone modifications, nucleosome occupancy, transcription factor bindings (CTCF), cell replication timing, DNA methylation, and GC content, following previous analyses ([Otlu et al., 2023](#)). Table 1 describes the $L = 11$ covariates considered, as well as their expected direction of effect on aggregate mutation rate based on the literature; see Section S1 for more background. Section S5.2 provides details on the preprocessing of these data, including binning each file at a 2kb resolution and filtering blacklisted regions. All covariates are centered and scaled to have mean zero and variance one along the genome.

5.1 DE NOVO ANALYSIS

We first perform a *de novo* analysis, that is, estimating all of the signatures without using reference signatures from COSMIC to inform priors or parameter values.

Computation. We use the PPF model with the default settings described in Section 2.4, setting $K = 12$ as an upper bound. We run Algorithm 1 from three different starting points generated at random via the initialization strategy in Section 4.2, stopping the updates when the relative difference in log-posterior falls below 10^{-7} . These runs took 1,379, 2,739, and 1,409 iterations to complete in parallel, over a total of 211, 367, and 215 minutes (average of 9 seconds per iterations), respectively, on an AMD Ryzen 3900-based dedicated server with 128GB of memory, running Ubuntu 20.04, R version 4.3.1 linked to Intel MKL 2019.5-075. All three runs detect very similar sets of signatures: the average cosine similarity between each pair of solutions is 0.9 after matching columns via the Hungarian algorithm. The estimated number of signatures \hat{K} (the number for which $\hat{\mu}_k^{\text{MAP}} > 1.5\varepsilon$) was 10, 9, and 9, respectively. We selected the solution with the highest log-posterior density as the initial value for Algorithm 2, and ran it for 10,000 iterations, using the last 3,000 to compute posterior means and 95% credible intervals. Our overall solution has $\hat{K} = 9$ signatures.

Interestingly, in a few cases, some signatures had relevance weight $\hat{\mu}_k^{\text{MAP}} \approx \varepsilon$, but $\hat{\beta}_k^{\text{MAP}}$ was not equal to zero. In contrast, we always found that $\hat{r}_{ik}^{\text{MCMC}} \approx 1/96$ (uniform) and $\hat{\beta}_k^{\text{MCMC}} \approx \mathbf{0}$ when $\hat{\mu}_k^{\text{MCMC}} \leq 1.5\varepsilon$. This

Table 1: Description of genomic and epigenetic covariates used in the application. The ASSAY column indicates the assay used to obtain the covariate. MUTATIONS describes previously reported associations between the covariate and mutation rate in cancer (not necessarily breast). The \nearrow and \searrow symbols indicate positive and negative effect, respectively. REFERENCE indicates the work that reports the association.

COVARIATE	ASSAY	DESCRIPTION AND ROLE	MUTATIONS	REFERENCE
Nucleosome occupancy	MNase-seq	Degree to which DNA is wrapped around nucleosomes; higher values indicate packed chromatin.	Periodic patterns	Pich et al. (2018)
H3K27ac	Histone ChIP-seq	Marker of active enhancers and promoters; associated with gene activation.	\nearrow	Schuster-Böckler and Lehner (2012)
H3K4me1	Histone ChIP-seq	Marks poised and active enhancers; enriched at regulatory elements.	\searrow	Hodgkinson et al. (2012)
H3K4me3	Histone ChIP-seq	Marks active promoters; associated with transcription initiation.	\searrow	Hodgkinson et al. (2012)
H3K9me3	Histone ChIP-seq	Marker of constitutive heterochromatin; gene silencing/repression.	\nearrow	Schuster-Böckler and Lehner (2012)
H3K27me3	Histone ChIP-seq	Repressive mark, associated with Polycomb-mediated gene silencing.	\nearrow	Schuster-Böckler and Lehner (2012)
H3K36me3	Histone ChIP-seq	Marker of transcriptional elongation within gene bodies.	\searrow	Li et al. (2013)
CTCF	TF ChIP-seq	Insulator protein, key architectural TF regulating chromatin looping and gene expression.	\nearrow	Katainen et al. (2015)
Replication timing	Repli-seq	Timing of DNA replication during S-phase of a cell; reflects chromatin state and genome organization.	\nearrow (later) \searrow (early)	Supek and Lehner (2015)
Methylation	WGBS	Level of DNA methylation; regulates gene expression and silencing.	\nearrow at CpGs	Bird (1980)
GC content	—	Proportion of G and C nucleotides a region; influences DNA stability and nucleosome positioning.	\searrow	Makova and Hardison (2015)

suggests that when $\hat{\mu}_k^{\text{MAP}} \approx \varepsilon$ but \hat{r}_k^{MAP} is not uniform or $\hat{\beta}_k^{\text{MAP}}$ is not near zero, it is likely a spurious artifact of the optimization.

Reconstruction error. To evaluate the fit in terms of aggregated counts, we compute the reconstruction error $\text{RMSE}(\hat{\Lambda}, N)$ where $N \in \mathbb{R}^{I \times J}$ is the matrix of total mutations from Section 2.1 and $\hat{\Lambda}$ is the expected value of this matrix under the estimated model, computed using Equation (5) with $A = [0, T]$. We compare this to the solutions from CompNMF (Zito and Miller, 2024) and SignatureAnalyzer (Kim et al., 2016), both of which also automatically select the number of signatures. PPF, CompNMF, and SignatureAnalyzer have reconstruction errors 14.01, 14.63, and 13.37, respectively, and estimated numbers of signatures 9, 5, and 9, respectively. Thus, PPF has comparable performance to methods designed to directly reconstruct the total counts. Moreover, PPF provides a region-specific fit as illustrated in Figure 3 (left), unlike CompNMF and SignatureAnalyzer, which are constant across the genome. Here, we compare our full model with a simpler version that uses copy numbers only, illustrating how using covariates substantially improves the reconstruction error at the Mb scale; see Figure 3 (right).

Signatures. Figure 4a reports the posterior mean and credible intervals for the signatures. Values in parentheses on the left indicate the closest COSMICv3.4 signature in terms of cosine similarity. We see that our model recovers both APOBEC-related signatures: Sig4 is a perfect match to SBS2, while Sig1 matches SBS13 in COSMICv3.4 with a score of 0.86, which however becomes 0.99 in COSMICv2, an earlier version of the database. Overall, the similarities are moderate-to-high, except for Sig8, whose similarity to SBS98 is too low for a confident match. Sig2 and Sig3 also have large contributions to the mutation rate, as demonstrated by the size of the relevance weights $\hat{\mu}_k$ in Figure 4b. Sig2 matches with SBS5, which is associated with aging, while Sig3 is close to SBS40A, which is ubiquitous in tumors (Alexandrov et al., 2020). Moreover, we find moderate

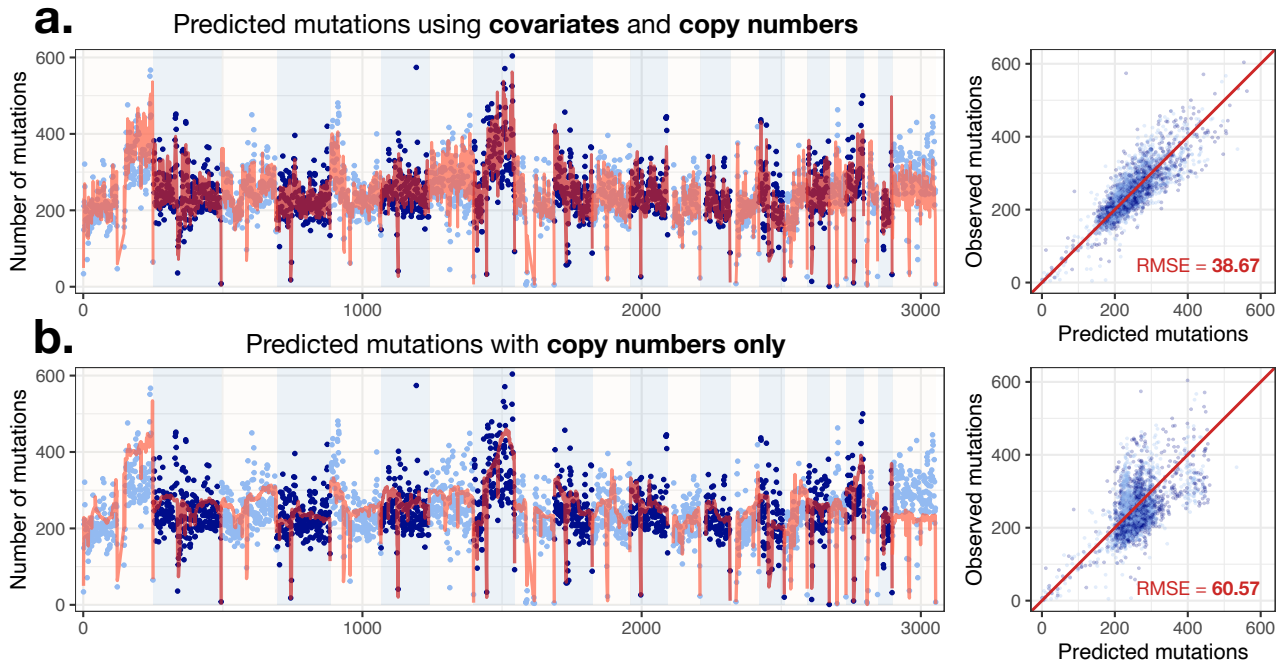


Figure 3: True and predicted total number of mutations from the PPF model at the megabase scale. Left: total mutations (points) and estimated total intensity (line); alternating colors and bands indicate chromosomes. Right: scatterplot of true and predicted values. **a.** PPF predictions using covariates from Table 1 and data on individual copy numbers. **b.** PPF predictions using individual copy numbers only, without covariates.

evidence of SBS3 (Sig5), SBS18 (Sig 7), and SBS10B (Sig9): these are important signatures in breast cancer, related to homologous recombination deficiencies (HRD), reactive oxygen species (ROS), and DNA replication proofreading, respectively.

Activities. Figure 4d shows the baseline activity of each signature in each patient, adjusted for copy number; this is computed as $\phi_{kj} \int_0^T \frac{1}{2} c_j(t) dt$. To understand the broader impact of each latent process, we perform a cluster analysis on a normalized version of these activities, selecting the optimal number of clusters by minimizing the silhouette score. This reveals three distinct groups: a large cluster characterized by relatively large rates of methylation-driven mutations and ROS damages (Cluster 1: Sig6 and Sig7), a medium-sized cluster with a high activity of SBS3 (Cluster 2: Sig5), and a small APOBEC-related cluster (Cluster 3: Sig1 and Sig4, and the hypermutated patients with Sig9). Notably, the SBS3 activity in Cluster 2 is indicative of HRD, for which PARP inhibition therapies have proven particularly effective (Gulhan et al., 2019).

Covariate effects. A central feature of the PPF model is its ability to associate location covariates with signatures. This is illustrated by Figure 4c, which shows the posterior means of the regression coefficients $\hat{\beta}_k$. Since we standardized the covariates, all values are on the same scale. Gray cells without numbers indicate coefficients that are not significantly different from zero, in the sense that their 95% posterior credible intervals contain zero. We highlight the following key findings.

1. Methylation covariate enables clean recovery of SBS1 and lowers the estimated mutation rates for C>A-enriched signatures. Signature Sig6 has a cosine similarity of 0.98 with SBS1, an almost perfect match. In turn, its coefficient for methylation is large and positive (0.42), which is consistent with the proposed biological mechanism, namely C>T mutations arising from methylated CpG sites. Meanwhile, CompNMF and SignatureAnalyzer recover contaminated versions of SBS1: CompNMF finds one signature that

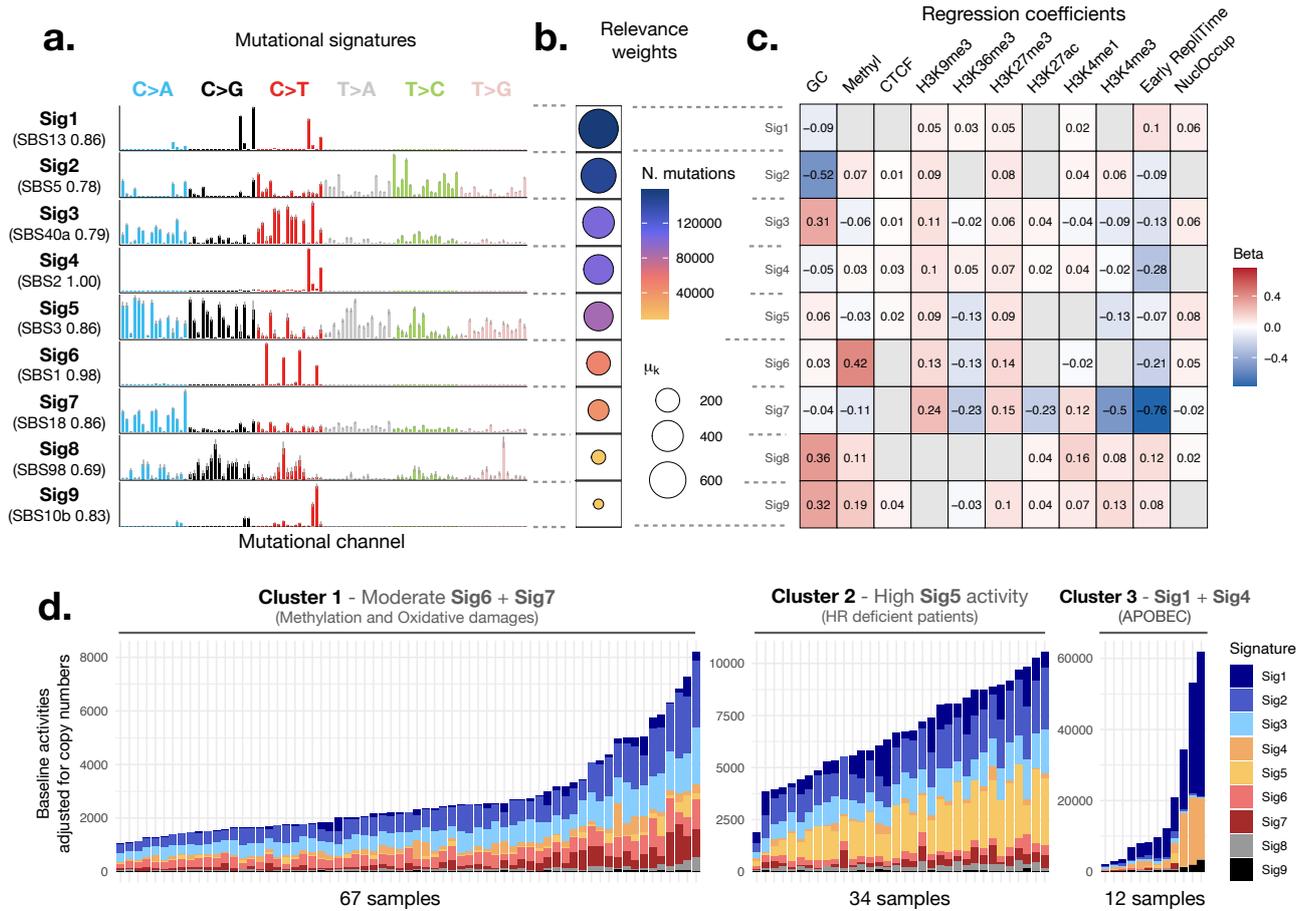


Figure 4: **a.** Posterior mean for the *de novo* mutational signatures, with gray bars indicating 95% credible intervals. Numbers in parentheses on the left indicate the highest cosine similarity in the COSMICv3.4 catalog. **b.** Posterior mean of the relevance weights $\hat{\mu}_k$ associated with each signature, with larger point size indicating larger values. Color intensity denotes the number of mutations in the data assigned to the signature via Equation (11). **c.** Posterior mean of the regression coefficients, $\hat{\beta}_k$. Gray cells with no number indicate estimates for which the 95% credible interval contains zero. **d.** Baseline activities $\hat{\theta}_{k,j}$ adjusted by total copy numbers. Columns correspond to patients, split by the clusters inferred from the normalized activities.

matches SBS1 with 0.82 cosine similarity, while SignatureAnalyzer finds two SBS1-like signatures with 0.83 and 0.80 similarity; see Figure S3. Contamination of SBS1 with other signatures, especially SBS5, is a common issue in many tools since their activities tend to be correlated (Wu et al., 2022). However, using methylation as a covariate appreciably mitigates this issue in our model. Interestingly, Sig3, Sig5, and Sig7, which all feature a high probability of C>A substitutions, are inversely associated with methylation. Since we are using 2kb binning with piecewise constant covariate values, this suggests that being in areas near methylated sites may lead to lower activities from other processes, particularly oxidative stress and HR deficiencies. More generally, GC content has a strong effect on several signatures, as reflected in the size of the coefficients in Sig2, Sig3, Sig8, and Sig9.

2. Late replication timing leads to large increases in mutational burden, but some signatures are more active in early replicating regions. The link between replication timing and overall mutation rate is well established (Dietzen et al., 2024). This covariate is defined such that higher values indicate earlier replication timing, which means that a negative $\beta_{k\ell}$ indicates enrichment in later replicating regions. Our

results indicate strong associations with several signatures, with Sig7, Sig4, and Sig6 being the most affected. Our estimates indicate that a one standard deviation increase in late replication timing translates to a 113% increase in the expected mutations due to oxidative damage (Sig7, $e^{0.76} - 1 \approx 1.13$), a 23% increase in SBS1 (Sig6, $e^{0.21} - 1 \approx 0.23$), and a 32% increase in the faulty APOBEC signature SBS2 (Sig 4, $e^{0.28} - 1 \approx 0.32$), holding all other covariates constant. In contrast, the other APOBEC-related signature, Sig1, shows decreased activity with later replication timing, with a 10% decrease per standard deviation.

Existing approaches like `SigProfilerTopography` (Otlu and Alexandrov, 2025) assess the impact of replication timing by tiling the total genomic signal into deciles and counting the number of mutations from a signature belonging to each bin. Then, these approaches test for a difference between this partition and the one obtained by placing mutations at random genomic locations. Mutations are typically assigned to a signature only if their attribution probability exceeds a certain threshold (e.g., 90%), leading to a loss of information. Our model-based approach jointly quantifies the covariate effects, adjusting for other covariates and copy numbers, without loss of information. Consequently, our results may differ from previously reported results in some cases: for instance, COSMIC reports that SBS10B is mildly enriched at later replicating areas in colorectal and endometrial cancer. In breast cancer, when controlling for several other covariates we find that our Sig9 (which matches to SBS10B) is mildly but positively associated with early replication.

3. All activities increase in heterochromatic domains and vary at active enhancers and promoters. H3K9me3 and H3K27me3, which are markers for heterochromatin and gene suppression, respectively, have nonnegative coefficients for every signature. H3K36me3 exhibits a mild positive association with APOBEC signatures Sig1 and Sig4 (exhibiting 3% and 5% increases per standard deviation, respectively). Meanwhile, we find that H3K36me3 has a strong inhibitory effect on Sig5, Sig6, and Sig7, which is consistent with its known role in recruiting mismatch repair factors and thus limiting the accumulation of replication-associated mismatches (Li et al., 2013). The effects of H3K4ac, H3K4me1, and H3K4me3, which are markers for enhancers and promoters and favor gene activity, differ across signatures. In particular, Sig7 and Sig5 are the most affected by H3K4me3. Finally, several signatures are slightly positively associated with the presence of CTCF sites. The small coefficients might be due to the 2kb aggregation, since individual TF’s are much smaller.

5.2 ANALYSIS USING PRE-SPECIFIED SIGNATURES

In this section, we take the signatures to be fixed and known based on a set of reference COSMIC signatures, and fit the rest of the parameters. This is commonly referred to as *signature refitting* analysis, and is often done using non-negative least squares. Since many COSMIC signatures have been linked to known biological processes, this can improve interpretability. By fixing the signatures, our PPF model can be used to implement a refitting approach that infers position-specific signature activities based on genomic covariates.

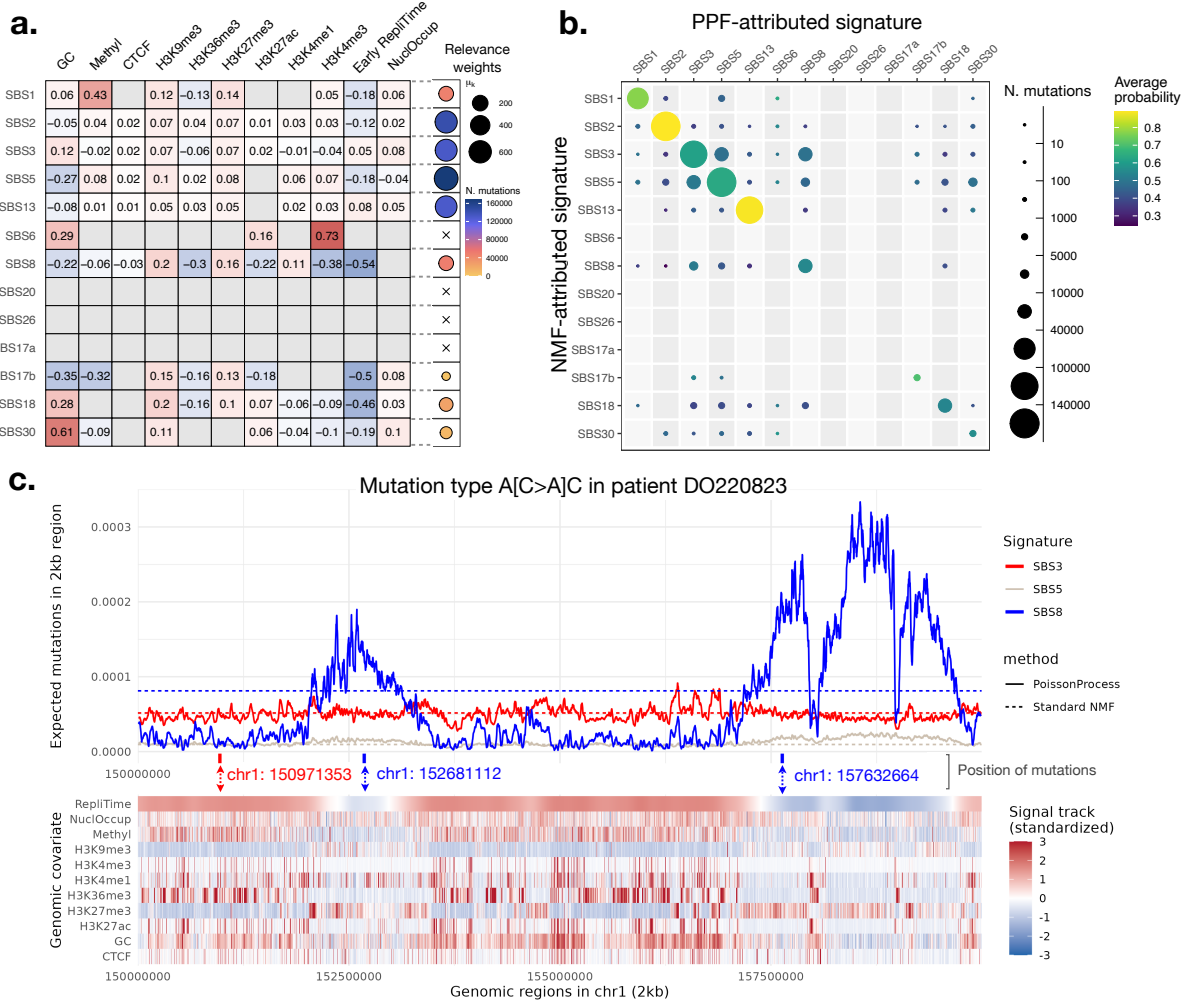


Figure 5: **a.** Regression coefficients and relevance weights for the signatures in the analysis. Gray boxes indicate entries where the 95% posterior credible interval contains zero. The \times marks indicate cases where $\hat{\mu}_k \approx \varepsilon$. **b.** Number of mutations attributed to a signature in the standard NMF case (y-axis) and in the PPF model (x-axis). **d.** Top panel: mutation intensity for SBS3, SBS5, and SBS8 on substitution type A[C>A]C in patient DO220823 in genomic region chr1:150000000-160000000. The three ticks indicate the exact mutation position. Solid and dashed lines indicate the intensity from the PPF and the CompNMF model with fixed signatures, respectively. Bottom: standardized values for the covariates in the region.

Model and computation. Consider a PPF with $K = 13$ and with the same covariates as in Table 1, but with r_1, \dots, r_K set to the following COSMICv3.4 signatures: two aging signatures (SBS1 and SBS5), two APOBEC-related signatures (SBS2 and SBS13), three associated with mismatch repair deficiencies (SBS6, SBS20, and SBS26), three related to oxidative damage (SBS18, SBS17A, and SBS17B), two HRD-related (SBS3 and SBS8), and one related to base excision repair deficiency (SBS30). A similar comparison was previously investigated by [Morganella et al. \(2016\)](#), who first explored their relationship with epigenetic marks in breast adenocarcinoma. We modify Algorithm 2 to skip the updates to the signatures r_k (Step 2), and run it for 10,000 iterations with randomly initialized activities, discarding the first 2,000 iterations as burn-in. We use the default PPF prior hyperparameters in Section 2.4.

Relevance weights and covariate effects. Figure 5a shows the posterior means of the regression coefficients $\hat{\beta}_k$ and the relevance weights $\hat{\mu}_k$. The “ \times ” mark shown for SBS6, SBS20, SBS26, and SBS17a indicates that

$\hat{\mu}_k \approx \varepsilon$. The regression coefficients of the last three signatures are estimated near zero after shrinkage, making the contribution of the corresponding signature negligible. A minor exception is SBS6, for which GC content, H3K27ac, and H3K4me3 have non-zero coefficients, even though $\hat{\mu}_k \approx \varepsilon$. The values of $\hat{\beta}_k$ for SBS1 closely resemble the estimates in the *de novo* results in Figure 4c, where Sig6 corresponds to SBS1. We find an increase in activity of SBS3 and SBS13 with an early replication timing, which differs from previous analyses (Morganella et al., 2016). For all signatures, we still detect increased mutation rates in association with heterochromatic markers H3K9me3 and H3K27me3, while the effect of H3K36me3 is varied but mostly negative. As before, the largest contributors are SBS2, SBS3, SBS5, and SBS13, and GC content exhibits relatively large effects. Finally, it is interesting to note that SBS8 and SBS17b have fairly strongly correlated coefficients. Signs are usually both positive or both negative. This suggests that SBS8 and SBS17b tend to be active in similar regions. Neither signature was detected in the previous analysis.

Attribution of mutations to signatures. An important aspect of the PPF model is that we can calculate mutation-specific signature attribution probabilities, as described in Section 3.2, and infer which signatures are most likely to have generated any given mutation. By comparison, in the baseline NMF model (Equation (1)), the attribution probabilities in Equation (11) are the same at every location t_{ijn} (for a given i, j, k). To quantify the benefit of using PPF, we fit the baseline NMF model using CompNMF (Algorithm S1) with the same set of fixed signatures, and compute the attribution probabilities for each mutation.

Figure 5b shows a cross-tabulation of the mutation attribution to each signature, by model, and the average assignment probabilities for these mutations. We see that the majority of attributions are consistent between the two models, as demonstrated by the large values on the main diagonal. However, 95,042 mutations (13.2% of the total) are estimated to have a different attribution, though the classification probabilities are lower on average.

Specific examples include differences in attributions to SBS3, SBS8, and, to a lesser extent, SBS5. The first two signatures show a similar pattern of mutations at C>A and T>A substitutions, which naturally leads to a higher *a priori* uncertainty in the attribution probability. SBS8 has been posited to originate from homologous recombination deficiencies Singh et al. (2020), but, unlike SBS3, experimental validation for this conjecture has not been achieved yet. In Figure 5c, which displays the posterior for the intensity function in region chr1:150000000-160000000 for patient DO220823 and mutation type $i = A[C > A]C$, we see that such unclear biological identification might be related to a higher propensity of SBS8 to appear in heterochromatic regions characterized by later replication timing. The three ticks between the facets indicate the genomic position where mutations were detected in the region. In the plot, we smooth the intensity using a rolling mean with a 10-region window to aid visualization. PPF attributes the first mutation to SBS3, since it falls in a region characterized by early replication timing, with strong peaks of H3K36me3 and low values of H3K9me3 and H3K27me3. Meanwhile, the other two mutations are detected in regions of predominantly late replication timing, leading PPF to attribute them to SBS8 due to the higher predicted activity of that signature. Interestingly, this activity drops dramatically when H3K36me3 is high, which explains the two dips in the predicted SBS8 activity following the third mutation. Hence, our results validate the propensity of SBS8 to appear in late-replicating heterochromatic regions Singh et al. (2020), demonstrating the advantages of the PPF framework.

6 DISCUSSION

Mutational signature analysis is now routinely performed in studies of tumors with whole-genome or whole-exome sequencing data, and remains an area of active methodological development. The method presented in this article further advances the state-of-the-art by introducing a model that enables joint inference on mutational signatures and their dependence on genomic features such as histone modifications, transcription factors, GC content, and DNA methylation, as well as patient-specific copy number alterations. Our analyses illustrate how adding covariates to the factorization improves interpretability, while also improving the detection of signatures. Furthermore, the model naturally provides position-specific activities for each signature, which allows one to infer which signature generated each observed mutation, based on genomic context and covariates. This helps in generating mechanistic hypotheses in a novel way compared to earlier methods.

In our model, signatures are held constant throughout the genome, whereas covariate-dependent activities capture regional variations. However, many COSMIC signatures display asymmetries with respect to replication strand (Otlu et al., 2023). This effect can be modeled by allowing signatures to depend on genomic coordinates, paired with, for instance, hierarchical Dirichlet priors over strand-specific hyperparameters.

Additionally, our analyses considered covariates from a reference epigenome common to all patients, with the exception of patient-specific copy numbers. However, epigenomes may show variability across individuals, tissues, and cell-specific chromatin domains (Gopi and Kidder, 2021). In such cases, our framework can be adapted to incorporate patient-specific genomic covariates such as chromatin accessibility (Corces et al., 2018) and patient-specific methylation, with associated patient-specific regression coefficients. Estimation of the model parameters would follow similar steps to the ones detailed in Section 3, though with increased computational costs. This extension has the potential to offer further insight into the mutational processes in cancer genomes, with the ultimate goal of improving precision therapies.

ACKNOWLEDGEMENTS

We are deeply grateful to Mehmet Samur, Jenna Landy, and Catherine Xue for the many helpful discussions. J.W. Miller and A. Zito were supported in part by the National Cancer Institute of the NIH under award number R01CA240299. G. Parmigiani and A. Zito were supported by grant number 5R01CA262710-05. The content is solely the responsibility of the authors and does not necessarily represent the official views of the National Institutes of Health. A. Zito also acknowledges support from Paula and Rodger Riney Foundation.

CODE AVAILABILITY

Code to run the method and reproduce the results in the article is publicly available at <https://github.com/alessandrozito/SigPoisProcess>.

REFERENCES

Abascal, F., R. Acosta, N. J. Addleman, et al. (2020). Expanded encyclopaedias of DNA elements in the human and mouse genomes. *Nature* 583(7818), 699–710.

- Aguirre, A. J., J. A. Nowak, N. D. Camarda, et al. (2018). Real-time genomic characterization of advanced pancreatic cancer to enable precision medicine. *Cancer Discovery* 8(9), 1096–1111.
- Alexandrov, L. B., P. H. Jones, D. C. Wedge, J. E. Sale, P. J. Campbell, S. Nik-Zainal, and M. R. Stratton (2015). Clock-like mutational processes in human somatic cells. *Nature Genetics* 47(12), 1402–1407.
- Alexandrov, L. B., J. Kim, N. J. Haradhvala, et al. (2020). The repertoire of mutational signatures in human cancer. *Nature* 578(7793), 94–101.
- Alexandrov, L. B., S. Nik-Zainal, D. C. Wedge, et al. (2013). Signatures of mutational processes in human cancer. *Nature* 500(7463), 415–421.
- Amemiya, H. M., A. Kundaje, and A. P. Boyle (2019). The ENCODE blacklist: Identification of problematic regions of the genome. *Scientific Reports* 9(1), 9354.
- Bird, A. P. (1980, 04). DNA methylation and the frequency of CpG in animal DNA. *Nucleic Acids Research* 8(7), 1499–1504.
- Blokzijl, F., R. Janssen, R. van Boxtel, and E. Cuppen (2018). MutationalPatterns: comprehensive genome-wide analysis of mutational processes. *Genome Medicine* 10(1), 33.
- Corces, M. R., J. M. Granja, S. Shams, et al. (2018). The chromatin accessibility landscape of primary human cancers. *Science* 362(6413), eaav1898.
- Daley, D. J. and D. Vere-Jones (2003). *An Introduction to the Theory of Point Processes. Vol. I* (Second ed.). Probability and its Applications (New York). New York.
- Dietzen, M., H. Zhai, O. Lucas, et al. (2024). Replication timing alterations are associated with mutation acquisition during breast and lung cancer evolution. *Nature Communications* 15(1), 6039.
- Dunson, D. B. and A. H. Herring (2005). Bayesian latent variable models for mixed discrete outcomes. *Biostatistics* 6(1), 11–25.
- Ernst, J. and M. Kellis (2017). Chromatin-state discovery and genome annotation with chromhmm. *Nature Protocols* 12(12), 2478–2492.
- Fischer, A., C. J. Illingworth, P. J. Campbell, and V. Mustonen (2013). EMu: probabilistic inference of mutational processes and their localization in the cancer genome. *Genome Biology* 14(4), R39.
- Gillis, N. (2020). *Nonnegative Matrix Factorization*.
- Gopi, L. K. and B. L. Kidder (2021). Integrative pan cancer analysis reveals epigenomic variation in cancer type and cell specific chromatin domains. *Nature Communications* 12(1), 1419.
- Gulhan, D. C., J. J.-K. Lee, G. E. M. Melloni, I. Cortés-Ciriano, and P. J. Park (2019). Detecting the mutational signature of homologous recombination deficiency in clinical samples. *Nature Genetics* 51(5), 912–919.

- Hansen, R. S., S. Thomas, R. Sandstrom, T. K. Canfield, R. E. Thurman, M. Weaver, M. O. Dorschner, S. M. Gartler, and J. A. Stamatoyannopoulos (2010). Sequencing newly replicated dna reveals widespread plasticity in human replication timing. *Proceedings of the National Academy of Sciences* 107(1), 139–144.
- Hodgkinson, A., Y. Chen, and A. Eyre-Walker (2012). The large-scale distribution of somatic mutations in cancer genomes. *Human Mutation* 33(1), 136–143.
- Hosseini, S. A., A. Khodadadi, K. Alizadeh, A. Arabzadeh, M. Farajtabar, H. Zha, and H. R. Rabiee (2020). Recurrent poisson factorization for temporal recommendation. *IEEE Transactions on Knowledge and Data Engineering* 32(1), 121–134.
- Islam, S. A., M. Díaz-Gay, Y. Wu, et al. (2022). Uncovering novel mutational signatures by de novo extraction with SigProfilerExtractor. *Cell Genomics* 2(11), 100179.
- Jaenisch, R. and A. Bird (2003). Epigenetic regulation of gene expression: how the genome integrates intrinsic and environmental signals. *Nature Genetics* 33(3), 245–254.
- Joe, H. (2006). Generating random correlation matrices based on partial correlations. *Journal of Multivariate Analysis* 97(10), 2177–2189.
- Katainen, R., K. Dave, E. Pitkänen, et al. (2015). CTCF/cohesin-binding sites are frequently mutated in cancer. *Nature Genetics* 47(7), 818–821.
- Kim, J., K. W. Mouw, P. Polak, et al. (2016). Somatic ERCC2 mutations are associated with a distinct genomic signature in urothelial tumors. *Nature Genetics* 48(6), 600–606.
- Kingman, J. F. C. (1993). *Poisson Processes*, Volume 3 of *Oxford Studies in Probability*. New York: Oxford University Press.
- Koh, G., A. Degasperis, X. Zou, S. Momen, and S. Nik-Zainal (2021). Mutational signatures: emerging concepts, caveats and clinical applications. *Nature Reviews Cancer* 21(10), 619–637.
- Last, G. and M. Penrose (2017). *Lectures on the Poisson Process*. Institute of Mathematical Statistics Textbooks. Cambridge University Press.
- Lawless, J. F. (1987). Regression methods for Poisson process data. *Journal of the American Statistical Association* 82(399), 808–815.
- Lawrence, M., R. Gentleman, and V. Carey (2009, 05). rtracklayer: an R package for interfacing with genome browsers. *Bioinformatics* 25(14), 1841–1842.
- Lawrence, M., W. Huber, H. Pagès, P. Aboyoun, M. Carlson, R. Gentleman, M. T. Morgan, and V. J. Carey (2013, 08). Software for computing and annotating genomic ranges. *PLoS Computational Biology* 9(8), 1–10.
- Lee, D. and H. S. Seung (2000). Algorithms for non-negative matrix factorization. In T. Leen, T. Dietterich, and V. Tresp (Eds.), *Advances in Neural Information Processing Systems*, Volume 13. MIT Press.

- Lee, D. D. and H. S. Seung (1999). Learning the parts of objects by non-negative matrix factorization. *Nature* 401(6755), 788–791.
- Lee, J., A. Lee, J.-K. Lee, J. Park, Y. Kwon, S. Park, H. Chun, Y. S. Ju, and D. Hong (2018, 05). Mutalisk: a web-based somatic mutation analysis toolkit for genomic, transcriptional and epigenomic signatures. *Nucleic Acids Research* 46(W1), W102–W108.
- Lee, S.-Y., H. Wang, H. J. Cho, R. Xi, and T.-M. Kim (2022). The shaping of cancer genomes with the regional impact of mutation processes. *Experimental & Molecular Medicine* 54(7), 1049–1060.
- Li, F., G. Mao, D. Tong, J. Huang, L. Gu, W. Yang, and G.-M. Li (2013). The histone mark H3K36me3 regulates human DNA mismatch repair through its interaction with MutSalpha. *Cell* 153(3), 590–600.
- Lloyd, C., T. Gunter, M. Osborne, S. Roberts, and T. Nickson (2016, 09–11 May). Latent point process allocation. In *Proceedings of the 19th International Conference on Artificial Intelligence and Statistics*, Volume 51, pp. 389–397.
- Loyfer, N., J. Magenheimer, A. Peretz, et al. (2023). A DNA methylation atlas of normal human cell types. *Nature* 613(7943), 355–364.
- Makova, K. D. and R. C. Hardison (2015). The effects of chromatin organization on variation in mutation rates in the genome. *Nature Reviews Genetics* 16(4), 213–223.
- Miller, A., L. Bornn, R. Adams, and K. Goldsberry (2014). Factorized point process intensities: A spatial analysis of professional basketball. In *Proceedings of the 31st International Conference on Machine Learning*, Volume 32, pp. 235–243.
- Miller, J. W. and S. L. Carter (2020). Inference in generalized bilinear models. arXiv:2010.04896.
- Morganella, S., L. B. Alexandrov, D. Glodzik, et al. (2016). The topography of mutational processes in breast cancer genomes. *Nature Communications* 7(1), 11383.
- Murray, I., R. Adams, and D. MacKay (2010). Elliptical slice sampling. In *Proceedings of the 13th International Conference on Artificial Intelligence and Statistics*, Volume 9, pp. 541–548.
- Nik-Zainal, S., L. B. Alexandrov, D. C. Wedge, et al. (2012). Mutational processes molding the genomes of 21 breast cancers. *Cell* 149(5), 979–993.
- Nishiyama, A. and M. Nakanishi (2021). Navigating the DNA methylation landscape of cancer. *Trends in Genetics* 37(11), 1012–1027.
- Otlu, B. and L. B. Alexandrov (2025). Evaluating topography of mutational signatures with SigProfilerTopography. *Genome Biology* 26(1), 134.
- Otlu, B., M. Díaz-Gay, I. Vermes, E. N. Bergstrom, M. Zhivagui, M. Barnes, and L. B. Alexandrov (2023). Topography of mutational signatures in human cancer. *Cell Reports* 42(8), 112930.

- Pagès, H., P. Aboyoun, R. Gentleman, and S. DebRoy (2023). *Biostrings: Efficient manipulation of biological strings*. R package version 2.68.1.
- Pich, O., F. Muiños, R. Sabarinathan, I. Reyes-Salazar, A. Gonzalez-Perez, and N. Lopez-Bigas (2018). Somatic and germline mutation periodicity follow the orientation of the DNA minor groove around nucleosomes. *Cell* 175(4), 1074–1087.e18.
- Polak, P., R. Karlič, A. Koren, et al. (2015). Cell-of-origin chromatin organization shapes the mutational landscape of cancer. *Nature* 518(7539), 360–364.
- Samur, M. K., A. Aktas Samur, M. Fulciniti, et al. (2020). Genome-wide somatic alterations in multiple myeloma reveal a superior outcome group. *Journal of Clinical Oncology* 38(27), 3107–3118.
- Schmalohr, C. L. (2025). *Modeling the Tissue-Specific Somatic Mutation Rate Along the Genome Based on Genomic Features*. Ph. D. thesis, Universität zu Köln.
- Schuster-Böckler, B. and B. Lehner (2012). Chromatin organization is a major influence on regional mutation rates in human cancer cells. *Nature* 488(7412), 504–507.
- Singh, V. K., A. Rastogi, X. Hu, Y. Wang, and S. De (2020). Mutational signature SBS8 predominantly arises due to late replication errors in cancer. *Communications Biology* 3(1), 421.
- Stamatoyannopoulos, J. A., I. Adzhubei, R. E. Thurman, G. V. Kryukov, S. M. Mirkin, and S. R. Sunyaev (2009). Human mutation rate associated with DNA replication timing. *Nature Genetics* 41(4), 393–395.
- Stratton, M. R., P. J. Campbell, and P. A. Futreal (2009). The cancer genome. *Nature* 458(7239), 719–724.
- Supek, F. and B. Lehner (2015). Differential DNA mismatch repair underlies mutation rate variation across the human genome. *Nature* 521(7550), 81–84.
- Supek, F. and B. Lehner (2019). Scales and mechanisms of somatic mutation rate variation across the human genome. *DNA Repair* 81, 102647.
- Tate, J. G., S. Bamford, H. C. Jubb, et al. (2018, 10). COSMIC: the Catalogue Of Somatic Mutations In Cancer. *Nucleic Acids Research* 47(D1), D941–D947.
- The ICGC/TCGA Pan-Cancer Analysis of Whole Genomes Consortium (2020). Pan-cancer analysis of whole genomes. *Nature* 578(7793), 82–93.
- Thurman, R. E., N. Day, W. S. Noble, and J. A. Stamatoyannopoulos (2007). Identification of higher-order functional domains in the human ENCODE regions. *Genome Research* 17(6), 917–927.
- Timmons, C., Q. Morris, and C. F. Harrigan (2022, 12). Regional mutational signature activities in cancer genomes. *PLOS Computational Biology* 18(12), 1–23.
- Tolstorukov, M. Y., N. Volfovsky, R. M. Stephens, and P. J. Park (2011). Impact of chromatin structure on sequence variability in the human genome. *Nature Structural & Molecular Biology* 18(4), 510–515.

- Vöhringer, H., A. V. Hoeck, E. Cuppen, and M. Gerstung (2021). Learning mutational signatures and their multidimensional genomic properties with TensorSignatures. *Nature Communications* 12(1), 3628.
- Wu, Y., E. H. Z. Chua, A. W. T. Ng, A. Boot, and S. G. Rozen (2022). Accuracy of mutational signature software on correlated signatures. *Scientific Reports* 12(1), 390.
- Zhou, M. and L. Carin (2015). Negative binomial process count and mixture modeling. *IEEE Transactions on Pattern Analysis and Machine Intelligence* 37(2), 307–320.
- Zito, A. and J. W. Miller (2024). Compressive Bayesian non-negative matrix factorization for mutational signatures analysis. arXiv:2404.10974.

SUPPLEMENTARY MATERIAL

“Poisson process factorization for mutational signature analysis with genomic covariates”

Section S1 provides details on the genomic covariates. Section S2 discusses recent work on the relationships between mutational signatures and epigenetic covariates. Section S3 provides proofs of the theoretical statements and contains a detailed derivation of the estimation and inference algorithms. Section S4 reports additional simulation results. Section S5 presents additional details and results for the breast adenocarcinoma application.

S1 ADDITIONAL DETAILS ON GENOMIC COVARIATES

Cellular activity is regulated by the interaction between the genome and the epigenome, largely through the action of molecular modifications that control DNA functions such as chromatin conformation, regulation of transcriptional activities of genes, and repair mechanisms (Jaenisch and Bird, 2003). To measure these activities at various genomic locations, an abundance of data has been collected from various assays and experiments over the last decade, with the Encyclopedia of DNA Elements (ENCODE; Abascal et al., 2020) being the largest publicly accessible collection in the field.

Nucleosome occupancy. The core building block of the spatial conformation of the genome is the nucleosome, a segment of 147 DNA base pairs wrapped around four pairs of histone proteins called H2A, H2B, H3, and H4. Nucleosomes are separated by 60-80 base pairs, forming “linker DNA”. Their relative position determines the type of chromatin in a given region and, subsequently, its accessibility. When nucleosomes are closely packed together—forming the heterochromatin—transcription is usually suppressed and DNA damage is harder to repair. In such regions, a higher frequency of somatic mutations has been observed in many cancers (Schuster-Böckler and Lehner, 2012). On the contrary, looser regions—comprising the euchromatin—exhibit fewer mutations (Polak et al., 2015). Current analyses suggest that mutational activity exhibits periodic patterns relating to nucleosome occupancy, with behaviors varying depending on the mutational signatures involved (Otlu et al., 2023). For background on the impact of chromatin conformation on mutations at the various scales, see Makova and Hardison (2015) and Supek and Lehner (2019).

Histone modifications and CTCF. The relative position and density of nucleosomes are influenced by histone modifications, which are chemical groups attached to certain proteins making up the histones. For instance, H3K36me3 indicates addition of three methyl groups (me3) on the lysine at position 36 (K36) in histone H3, causing elongations and favoring accessibility (Li et al., 2013). On the contrary, H3K9ac is short for addition of an acetyl group (ac) on the lysine at position 9 in H3, and is associated with gene activation. Depending on the modification at play, genomic regions can have higher or lower mutational burden; see Table 1. Genomic architecture is also shaped by sequence-specific DNA-binding proteins such as the transcription factor CTCF, which acts as an insulator and helps organize chromatin loops and domains. Previous analyses of cancer genomes showed increased mutation rates in CTCF binding sites (Katainen et al., 2015). Both CTCF and histone modifications are measured via chromatin immunoprecipitation (ChIP-seq assay).

Replication timing. Another important factor is the timing of DNA replication during the S-phase of the cell cycle (Thurman et al., 2007). Early replicating regions are usually populated with genes and are highly accessible, while late replicating regions tend to be heterochromatic (Stamatoyannopoulos et al., 2009).

Replication timing is estimated via Repli-seq (Hansen et al., 2010), which labels and sequences DNA synthesized at different stages of S-phase; timing values are computed by smoothing a weighted average of the proportion of early and late replicating cells in 1kb windows. By construction, low values of replication timing indicate that the region tends to replicate later, while high values denote regions that replicate early. Late-replicating regions tend to be more prone to mutation (Otlu et al., 2023).

Methylation and GC content. DNA methylation refers to the binding of a methyl group to a CpG locus (that is, C followed by G), forming 5-methylcytosine. This configuration is prone to spontaneous deamination, causing a C>T substitution (Nishiyama and Nakanishi, 2021). This mechanism is a common cause of DNA mutations (Bird, 1980). This mutational process is represented by the signature SBS1 in COSMIC, which is active in essentially all subjects and correlates with age (Alexandrov et al., 2015). Finally, the proportion of G and C nucleotides in a given genomic region—referred to as GC content—is associated with several important genomic and epigenomic features, including gene expression levels, chromatin accessibility, and replication timing. The total GC content in the hg19 reference genome is around 40%, but regions may peak at 80% at the kilobase scale.

S2 PREVIOUS WORK RELATING SIGNATURES TO EPIGENETICS

There are a few methods that investigate the regional variations in mutational signatures and their relationships with genomic features. In this section, we briefly describe them and discuss how they differ from our proposed method.

An early contribution in this direction is EMu Fischer et al. (2013), which infers region-specific signatures and activities by dividing the genome into megabase regions and fitting a separate NMF for each bin. More recently, GenomeTrackSig (Timmons et al., 2022) detects regional variation in signature activities by partitioning the genome into bins, and then performing a changepoint detection analysis. Each bin is recommended to have at least 100 mutations. However, neither method incorporates genomic covariates into the model.

A step in this direction is taken by TensorSignatures (Vöhringer et al., 2021), which applies Tucker-like factorizations to a tensor of mutations categorized into mutually exclusive chromatin states according to their position (Ernst and Kellis, 2017). However, TensorSignatures cannot leverage continuous covariates in the factorization. Moreover, benchmarking analyses indicated a need for improved performance (Islam et al., 2022).

Recently, a compendium of the topographical features related to each signature has been assembled by Otlu et al. (2023) and subsequently by Otlu and Alexandrov (2025) using the SigProfilerTopography software. Their goal is to test for enrichment or depletion of mutations in the proximity of given topographic marks, by comparing the observed mutation data against simulated mutations placed uniformly at random along the genome. This is, however, a *post hoc* analysis tool: each mutation in a patient is assigned to a specific signature without accounting for the covariates, and then values for each covariate are averaged by position using a 2kb window centered around the mutations. Hence, the method is useful for testing the aggregate effects of individual topographic marks, but not their joint effect on the mutation rate. Moreover, the method considers only the subsets of mutations that are attributed to a signature with high confidence, i.e. 0.90 attribution probability.

Additional *post hoc* analyses on the regional variations in mutational signatures and their association with genomic covariates are described by [Blokzijl et al. \(2018\)](#), [Lee et al. \(2018, 2022\)](#), and [Schmalohr \(2025\)](#). In all cases, these existing approaches consider a pre-estimated set of signatures and activities when inferring these associations. To our knowledge, no previous method in the literature performs estimation of the latent structure while also inferring the effect of genomic covariates in a joint model.

S3 PROOFS AND DERIVATIONS

S3.1 PROOFS OF THE STATEMENTS

Proof of Proposition 1. By assumption, $\vartheta_{kj}(t) = \theta_{kj}/T$, so Equation (3) becomes $\lambda_{ij}(t) = \sum_{k=1}^K r_{ik}\theta_{kj}/T$ for all t . It follows that $\int_0^T \lambda_{ij}(t)dt = \sum_{k=1}^K r_{ik}\theta_{kj}$ under this assumption. Therefore, the likelihood function in Equation (2) becomes

$$\begin{aligned} \mathcal{L}(\lambda) &= \prod_{i=1}^I \prod_{j=1}^J \left[\exp\left(-\int_0^T \lambda_{ij}(t)dt\right) \prod_{n=1}^{N_{ij}} \lambda_{ij}(t_{ijn}) \right] \\ &= \prod_{i=1}^I \prod_{j=1}^J \left[\exp\left(-\sum_{k=1}^K r_{ik}\theta_{kj}\right) \left(\sum_{k=1}^K r_{ik}\theta_{kj}/T\right)^{N_{ij}} \right] \\ &\propto \exp\left(-\sum_{j=1}^J \sum_{k=1}^K \theta_{kj}\right) \prod_{i=1}^I \prod_{j=1}^J \left(\sum_{k=1}^K r_{ik}\theta_{kj}\right)^{N_{ij}} \end{aligned}$$

since $\sum_{i=1}^I r_{ik} = 1$, where the proportionality is as a function of r_{ik} and θ_{kj} . This, in turn, is proportional to the likelihood function for the Poisson NMF model in Equation (1). \square

Proof of Proposition 2. The result follows from the superposition theorem of Poisson processes. See Theorem 3.3 in [Last and Penrose \(2017\)](#). \square

S3.2 DERIVATION OF MAP ESTIMATION ALGORITHM FOR PPF

We present a detailed derivation of the majorization-minimization strategy used to obtain Algorithm 1. By Equation (10),

$$\begin{aligned} -\log \pi(R, \Phi, B, \mu, \sigma^2 \mid \mathbf{t}) &= \tag{S1} \\ &= \sum_{jk} \phi_{kj} \int_0^T \frac{1}{2} c_j(t) e^{\beta_k^\top \mathbf{x}(t)} dt - \sum_{ij} \sum_{n=1}^{N_{ij}} \log \left(\sum_{k=1}^K r_{ik} \phi_{kj} \frac{1}{2} c_j(t_{ijn}) e^{\beta_k^\top \mathbf{x}(t_{ijn})} \right) \tag{Log-likelihood} \\ &\quad - \sum_{ik} (\alpha_{ik} - 1) \log r_{ik} \tag{Signatures} \\ &\quad - \sum_{jk} \left(-a \log \mu_k + (a-1) \log \phi_{kj} - \phi_{kj} \frac{a}{\mu_k} \int_0^T \frac{1}{2} c_j(t) dt \right) \tag{Baseline activities} \\ &\quad - \sum_k \left(-\frac{L}{2} \log \sigma_k^2 - \frac{1}{2\sigma_k^2} \beta_k^\top \beta_k \right) \tag{Regression coefficients} \end{aligned}$$

$$\begin{aligned}
& - \sum_k \left(- (a_0 + 1) \log \mu_k - \frac{b_0}{\mu_k} \right) && \text{(Relevance weights)} \\
& - \sum_k \left(- (c_0 + 1) \log \sigma_k^2 - \frac{d_0}{\sigma_k^2} \right) && \text{(Variances)} \\
& + \text{const}
\end{aligned}$$

subject to $\sum_{i=1}^I r_{ik} = 1$ for each $k = 1, \dots, K$. For generality, we consider the case of a generic hyperprior $\mu_k \sim \text{InvGa}(a_0, b_0)$ on the relevance weights; our compressive hyperprior in Equation (7) is recovered by letting $a_0 = aJ + 1$ and $b_0 = \varepsilon aJ$. The following result will be useful for our derivations.

Lemma 1. *Suppose $f : \mathcal{X} \rightarrow \mathbb{R}$ such that*

$$f(x) = - \log \sum_{k=1}^K h_k(x)$$

where $h_k(x) > 0$ is a strictly positive function for each $k = 1, \dots, K$. For $x, \tilde{x} \in \mathcal{X}$, define

$$g(x, \tilde{x}) = - \sum_{k=1}^K w_k(\tilde{x}) \log \frac{h_k(x)}{w_k(\tilde{x})}$$

where $w_k(x) = h_k(x) / \sum_{s=1}^K h_s(x)$. Then $f(x) \leq g(x, \tilde{x})$ and $f(x) = g(x, x)$ for all $x, \tilde{x} \in \mathcal{X}$.

In other words, the conclusion of Lemma 1 is that $g(x, \tilde{x})$ is a majorizer of $f(x)$. This provides a useful general strategy for obtaining majorizers of objective functions that involve a sum inside a logarithm.

Proof. The inequality $f(x) \leq g(x, \tilde{x})$ is a direct consequence of Jensen's inequality:

$$f(x) = - \log \sum_k w_k(\tilde{x}) \frac{h_k(x)}{w_k(\tilde{x})} \leq \sum_k w_k(\tilde{x}) \left(- \log \frac{h_k(x)}{w_k(\tilde{x})} \right) = g(x, \tilde{x})$$

since $-\log(x)$ is convex. The equality $f(x) = g(x, x)$ holds since, by the definition of $w_k(x)$,

$$g(x, x) = - \sum_k w_k(x) \log \frac{h_k(x)}{w_k(x)} = - \sum_k w_k(x) \log \sum_s h_s(x) = - \log \sum_s h_s(x) = f(x).$$

□

S3.2.1 DERIVATION OF STEP 1 - SIGNATURES

The update to the signature matrix R is obtained via a majorization-minimization step on Equation (S1) with respect to R , subject to the constraint that $\sum_i r_{ik} = 1$ for all k . Keeping only terms that depend on R , the objective function in Equation (S1) becomes

$$f(R) = - \sum_{ij} \sum_{n=1}^{N_{ij}} \log \left(\sum_{k=1}^K r_{ik} \phi_{kj} e^{\beta_k^\top \mathbf{x}(t_{ijn})} \right) - \sum_{ik} (\alpha_{ik} - 1) \log r_{ik},$$

noting that $\frac{1}{2} c_j(t_{ijn})$ comes out in a term that does not depend on R . To form a majorizer $g(R, \tilde{R})$ as a function of signature matrices R and \tilde{R} , we apply Lemma 1 for each i, j , and n , with $h_{ijnk}(R) = r_{ik}\phi_{kj}e^{\beta_k^\top \mathbf{x}(t_{ijn})}$ and $w_{ijnk}(R) = h_{ijnk}(R)/\sum_s h_{ijns}(R)$. Specifically, defining

$$g(R, \tilde{R}) = - \sum_{ijk} \sum_{n=1}^{N_{ij}} w_{ijnk}(\tilde{R}) \log \left(\frac{1}{w_{ijnk}(\tilde{R})} r_{ik}\phi_{kj} e^{\beta_k^\top \mathbf{x}(t_{ijn})} \right) - \sum_{ik} (\alpha_{ik} - 1) \log r_{ik},$$

it follows that $g(R, \tilde{R})$ is a majorizer of $f(R)$ by Lemma 1. To minimize $g(R, \tilde{R})$ with respect to each column r_k , we use the method of Lagrange multipliers. Define

$$\mathcal{L}(R) = g(R, \tilde{R}) - \tau \left(1 - \sum_i r_{ik} \right),$$

where τ is a Lagrange multiplier for the constraint $\sum_{i=1}^I r_{ik} = 1$. Differentiating $\mathcal{L}(R)$ with respect to r_{ik} and setting the derivative to 0 yields

$$0 = \frac{\partial \mathcal{L}(R)}{\partial r_{ik}} = - \sum_j \sum_{n=1}^{N_{ij}} \frac{w_{ijnk}(\tilde{R})}{r_{ik}} - \frac{\alpha_{ik} - 1}{r_{ik}} + \tau$$

for $i = 1, \dots, I$, or equivalently,

$$r_{ik} = \frac{1}{\tau} \left(\alpha_{ik} - 1 + \sum_j \sum_{n=1}^{N_{ij}} w_{ijnk}(\tilde{R}) \right) = \frac{1}{\tau} \left(\alpha_{ik} - 1 + \sum_j \sum_{n=1}^{N_{ij}} \frac{\tilde{r}_{ik}\phi_{kj}e^{\beta_k^\top \mathbf{x}(t_{ijn})}}{\sum_s \tilde{r}_{is}\phi_{sj}e^{\beta_s^\top \mathbf{x}(t_{ijn})}} \right).$$

Taking the derivative with respect to the Lagrange multiplier leads to $\sum_{i=1}^I r_{ik} = 1$. Plugging in this constraint and solving for τ yields the update in Algorithm 1, viewing \tilde{r}_k as the current value and r_k as the updated value.

S3.2.2 DERIVATION OF STEP 2 - BASELINE ACTIVITY

The update to the baseline activity matrix Φ is obtained via a majorization-minimization step on Equation (S1) with respect to Φ . Keeping only terms that depend on Φ , the objective function in Equation (S1) becomes

$$\begin{aligned} f(\Phi) &= \sum_{jk} \phi_{kj} \int_0^T \frac{1}{2} c_j(t) e^{\beta_k^\top \mathbf{x}(t)} dt - \sum_{ij} \sum_{n=1}^{N_{ij}} \log \left(\sum_{k=1}^K r_{ik}\phi_{kj} e^{\beta_k^\top \mathbf{x}(t_{ijn})} \right) \\ &\quad - \sum_{jk} \left((a-1) \log \phi_{kj} - \phi_{kj} \frac{a}{\mu_k} \int_0^T \frac{1}{2} c_j(t) dt \right). \end{aligned}$$

We use the same majorization trick as in Step 1, with $h_{ijnk}(\Phi)$ and $w_{ijnk}(\Phi)$ defined the same way but viewed as functions of Φ . This yields the majorizer

$$g(\Phi, \tilde{\Phi}) = \sum_{jk} \phi_{kj} \int_0^T \frac{1}{2} c_j(t) e^{\beta_k^\top \mathbf{x}(t)} dt - \sum_{ijk} \sum_{n=1}^{N_{ij}} w_{ijnk}(\tilde{\Phi}) \log \left(\frac{1}{w_{ijnk}(\tilde{\Phi})} r_{ik}\phi_{kj} e^{\beta_k^\top \mathbf{x}(t_{ijn})} \right)$$

$$- \sum_{jk} \left((a-1) \log \phi_{kj} - \phi_{kj} \frac{a}{\mu_k} \int_0^T \frac{1}{2} c_j(t) dt \right).$$

To minimize $g(\Phi, \tilde{\Phi})$ with respect to ϕ_{kj} , we take the derivative and set it to zero:

$$0 = \frac{\partial g(\Phi, \tilde{\Phi})}{\partial \phi_{kj}} = \int_0^T \frac{1}{2} c_j(t) e^{\beta_k^\top \mathbf{x}(t)} dt - \sum_i \sum_{n=1}^{N_{ij}} \frac{w_{ijnk}(\tilde{\Phi})}{\phi_{kj}} - \left(\frac{a-1}{\phi_{kj}} - \frac{a}{\mu_k} \int_0^T \frac{1}{2} c_j(t) dt \right).$$

Solving for ϕ_{kj} and plugging in the definition of $w_{ijnk}(\tilde{\Phi})$, we have

$$\begin{aligned} \phi_{kj} &= \frac{a-1 + \sum_i \sum_{n=1}^{N_{ij}} w_{ijnk}(\tilde{\Phi})}{\int_0^T \frac{1}{2} c_j(t) e^{\beta_k^\top \mathbf{x}(t)} dt + (a/\mu_k) \int_0^T \frac{1}{2} c_j(t) dt} \\ &= \left(a-1 + \sum_i \sum_{n=1}^{N_{ij}} \frac{r_{ik} \tilde{\phi}_{kj} e^{\beta_k^\top \mathbf{x}(t_{ijn})}}{\sum_s r_{is} \tilde{\phi}_{sj} e^{\beta_s^\top \mathbf{x}(t_{ijn})}} \right) \left(\int_0^T \frac{1}{2} c_j(t) (e^{\beta_k^\top \mathbf{x}(t)} + a/\mu_k) dt \right)^{-1}, \end{aligned}$$

which yields the update in Algorithm 1, treating $\tilde{\Phi}$ as the current value and Φ as the updated value. In this case, there is need to use Lagrange multipliers, since the only constraint is that $\phi_{kj} > 0$, which is guaranteed as long as $a > 1$.

S3.2.3 DERIVATION OF STEP 3 - REGRESSION COEFFICIENTS

Following the same approach as in Step 2, but for B , the objective function in Equation (S1) becomes

$$f(B) = \sum_{jk} \phi_{kj} \int_0^T \frac{1}{2} c_j(t) e^{\beta_k^\top \mathbf{x}(t)} dt - \sum_{ij} \sum_{n=1}^{N_{ij}} \log \left(\sum_{k=1}^K r_{ik} \phi_{kj} e^{\beta_k^\top \mathbf{x}(t_{ijn})} \right) + \sum_k \frac{1}{2\sigma_k^2} \beta_k^\top \beta_k$$

and the majorizer is

$$g(B, \tilde{B}) = \sum_{jk} \phi_{kj} \int_0^T \frac{1}{2} c_j(t) e^{\beta_k^\top \mathbf{x}(t)} dt - \sum_{ij} \sum_{n=1}^{N_{ij}} w_{ijnk}(\tilde{B}) \log \left(\frac{r_{ik} \phi_{kj} e^{\beta_k^\top \mathbf{x}(t_{ijn})}}{w_{ijnk}(\tilde{B})} \right) + \sum_k \frac{1}{2\sigma_k^2} \beta_k^\top \beta_k,$$

where

$$w_{ijnk}(B) = \frac{r_{ik} \phi_{kj} e^{\beta_k^\top \mathbf{x}(t_{ijn})}}{\sum_s r_{is} \phi_{sj} e^{\beta_s^\top \mathbf{x}(t_{ijn})}}.$$

To minimize $g(B, \tilde{B})$ over β_k , we use a Newton's method step as follows. The gradient and Hessian of $g(B, \tilde{B})$ with respect to β_k are

$$\begin{aligned} \mathbf{g}_k &= \sum_j \phi_{kj} \int_0^T \frac{1}{2} c_j(t) e^{\beta_k^\top \mathbf{x}(t)} \mathbf{x}(t) dt - \sum_{ij} \sum_{n=1}^{N_{ij}} w_{ijnk}(\tilde{B}) \mathbf{x}(t_{ijn}) + \frac{1}{\sigma_k^2} \beta_k \\ \mathbf{H}_k &= \sum_j \phi_{kj} \int_0^T \frac{1}{2} c_j(t) e^{\beta_k^\top \mathbf{x}(t)} \mathbf{x}(t) \mathbf{x}(t)^\top dt + \frac{1}{\sigma_k^2} I_L. \end{aligned}$$

Treating \tilde{B} as the current value, a Newton step would be to update β_k to $\tilde{\beta}_k - \mathbf{H}_k^{-1} \mathbf{g}_k$, evaluating \mathbf{g}_k and \mathbf{H}_k at $\beta_k = \tilde{\beta}_k$. This leads to the update in Algorithm 1. As discussed in Section 3.1, for numerical stability, we modify this to use the correction proposed by [Miller and Carter \(2020\)](#).

S3.2.4 DERIVATION OF STEP 4 - RELEVANCE WEIGHTS AND VARIANCE PARAMETERS

The updates for μ_k and σ_k^2 are derived by analytically maximizing the log posterior density. Keeping only the terms that depend on μ_k , the objective function in Equation (S1) becomes

$$\begin{aligned} f(\mu_k) &= - \sum_j \left(-a \log \mu_k - \phi_{kj} \frac{a}{\mu_k} \int_0^T \frac{1}{2} c_j(t) dt \right) - \left(-(a_0 + 1) \log \mu_k - \frac{b_0}{\mu_k} \right) \\ &= (a_0 + aJ + 1) \log \mu_k + \left(b_0 + a \sum_j \phi_{kj} \int_0^T \frac{1}{2} c_j(t) dt \right) \frac{1}{\mu_k}. \end{aligned}$$

Since $\exp(-f(\mu_k)) \propto \text{InvGa}(\mu_k | a_0 + aJ, b_0 + a \sum_j \phi_{kj} \int_0^T \frac{1}{2} c_j(t) dt)$, the minimizer of $f(\mu_k)$ is the mode of this inverse gamma distribution, namely,

$$\mu_k = \frac{b_0 + a \sum_j \phi_{kj} \int_0^T \frac{1}{2} c_j(t) dt}{a_0 + aJ + 1}.$$

Our choices of $a_0 = aJ + 1$ and $b_0 = \varepsilon aJ$ yield the update in Algorithm 1.

Likewise, keeping only the terms that depend on σ_k^2 , the objective function becomes

$$\begin{aligned} f(\sigma_k^2) &= - \left(-\frac{L}{2} \log \sigma_k^2 - \frac{1}{2\sigma_k^2} \beta_k^\top \beta_k \right) - \left(-(c_0 + 1) \log \sigma_k^2 - \frac{d_0}{\sigma_k^2} \right) \\ &= \left(c_0 + \frac{L}{2} + 1 \right) \log \sigma_k^2 + \left(d_0 + \frac{1}{2} \beta_k^\top \beta_k \right) \frac{1}{\sigma_k^2}. \end{aligned}$$

Since $\exp(-f(\sigma_k^2)) \propto \text{InvGa}(\sigma_k^2 | c_0 + L/2, d_0 + \beta_k^\top \beta_k/2)$, the minimizer of $f(\sigma_k^2)$ is

$$\sigma_k^2 = \frac{d_0 + \beta_k^\top \beta_k/2}{c_0 + L/2 + 1},$$

which is the update in Algorithm 1.

S3.3 DERIVATION OF MCMC ALGORITHM FOR PPF

The likelihood function is

$$\mathcal{L} = \exp \left(- \sum_{jk} \int_0^T \frac{1}{2} c_j(t) \phi_{kj} e^{\beta_k^\top \mathbf{x}(t)} dt \right) \prod_{ij} \prod_{n=1}^{N_{ij}} \left(\sum_{k=1}^K \frac{1}{2} c_j(t_{ijn}) r_{ik} \phi_{kj} e^{\beta_k^\top \mathbf{x}(t_{ijn})} \right).$$

We adopt a data augmentation approach typical of Poisson factorization ([Dunson and Herring, 2005](#)). Specifically, we introduce a multinomial random variable for each of the observed mutations such that

$$W_{ij}(t_{ijn}) = (W_{ij1}(t_{ijn}), \dots, W_{ijK}(t_{ijn})) \sim \text{Mult}(1; p_{ij1}(t_{ijn}), \dots, p_{ijK}(t_{ijn})),$$

where

$$p_{ijk}(t_{ijn}) = \mathbb{P}(W_{ijk}(t_{ijn}) = 1 \mid R, \Phi, B, \mathbf{t}) = \frac{r_{ik}\phi_{kj}e^{\beta_k^\top \mathbf{x}(t_{ijn})}}{\sum_{s=1}^K r_{is}\phi_{sj}e^{\beta_s^\top \mathbf{x}(t_{ijn})}}.$$

Then one can write the augmented posterior as

$$\begin{aligned} \pi(R, \Phi, B, \mu, \sigma^2, W \mid \mathbf{t}) &\propto && \text{(S2)} \\ &\propto \exp\left(-\sum_{jk} \phi_{kj} \int_0^T \frac{1}{2} c_j(t) e^{\beta_k^\top \mathbf{x}(t)} dt\right) \prod_{ij} \prod_{n=1}^{N_{ij}} \prod_k \left(\frac{1}{2} c_j(t_{ijn}) r_{ik} \phi_{kj} e^{\beta_k^\top \mathbf{x}(t_{ijn})}\right)^{W_{ijk}(t_{ijn})} && \text{(Likelihood)} \\ &\times \prod_k \prod_i r_{ik}^{\alpha_{ik}-1} && \text{(Signatures)} \\ &\times \prod_k \prod_j \mu_k^{-a} \phi_{kj}^{a-1} \exp\left(-\phi_{kj} \frac{a}{\mu_k} \int_0^T \frac{1}{2} c_j(t) dt\right) && \text{(Activities)} \\ &\times \prod_k (\sigma_k^2)^{-L/2} \exp\left(-\frac{1}{2\sigma_k^2} \beta_k^\top \beta_k\right) && \text{(Coefficients)} \\ &\times \prod_k \mu_k^{-a_0-1} \exp(-b_0/\mu_k) && \text{(Weights)} \\ &\times \prod_k (\sigma_k^2)^{-c_0-1} \exp(-d_0/\sigma_k^2). && \text{(Variances)} \end{aligned}$$

All the full conditionals in Algorithm 2 are standard conjugate updates based on Equation (S2). The β_k update is done using elliptical slice sampling (Murray et al., 2010) as described in Section 3.2.

S3.4 MAP FOR POISSON NMF WITH COMPRESSIVE HYPERPRIORS

The CompNMF model of Zito and Miller (2024) is a special case of the PPF model where $\beta_k = \mathbf{0}$, $c_j(t) = 2$, and $\phi_{kj} = \theta_{kj}/T$ for all j, k, t , since then $\vartheta_{kj}(t) = \theta_{kj}/T$ and Proposition 1 applies. Hence, the *maximum a posteriori* (MAP) estimate can be obtained using the same steps as Algorithm 1. Notice that these steps are valid if $a \geq 1$ and $\alpha_{ik} \geq 1$.

The following algorithm reduces Algorithm 1 to this special case, which yields a MAP algorithm for the baseline Poisson NMF model in Equation (1) with automatic selection of the number of factors. Unlike the PPF algorithm, these updates can be written using matrix multiplication operations, which are particularly fast. We stop the algorithm when two successive iterations of the log posterior density have a relative difference less than 10^{-7} . The compressive hyperprior is obtained by using $a_0 = aJ + 1$ and $b_0 = \varepsilon aJ$.

Algorithm S1. MAP updates for CompNMF

Input: Count matrix N , where N_{ij} = number of mutations of type i in patient j .

1 **Signatures:** Update the signature matrix R as

$$R \leftarrow \text{normalize} \left((A - 1) + R \circ \left(\frac{N}{R\Theta} \Theta^\top \right) \right)$$

where $A = (\alpha_{ik}) \in \mathbb{R}^{I \times K}$ is the matrix with (i, j) entry α_{ik} . Here, \circ denotes element-wise multiplication (Hadamard product), $\frac{X}{R\Theta}$ is element-wise division, and $\text{normalize}(\cdot)$ makes each column of R sum to one.

2 **Activities:** Let $\mu = (\mu_1, \dots, \mu_K)$ be the vector of relevance weights, and let M be the $K \times J$ matrix with every column equal to μ . Update the activity matrix Θ as

$$\Theta \leftarrow \left((a - 1) + \Theta \circ \left(R^\top \frac{N}{R\Theta} \right) \right) \circ \left(\frac{M}{a + M} \right).$$

3 **Relevance weights:** Update each relevance weight μ_k as

$$\mu_k \leftarrow \frac{b_0 + a \sum_{j=1}^J \theta_{kj}}{a_0 + aJ + 1}.$$

Output: Updated point estimates for R , Θ , μ .

S4 ADDITIONAL DETAILS ON THE SIMULATIONS

S4.1 DETAILS OF SIMULATION SETUP

The simulated covariates, copy numbers, true model parameters, and mutation data were generated as follows for each dataset.

Covariates. We set $T = 200,000$ and divide $[0, T)$ into equally sized bins $[\tau_m, \tau_{m+1})$ of length $\tau_{m+1} - \tau_m = 100$, so that $[0, T) = \bigcup_{m=1}^{M-1} [\tau_m, \tau_{m+1})$ with $M = 2000$, $\tau_1 = 0$, and $\tau_M = T$. We simulate autocorrelated signals as $\xi_m \sim N(D\xi_{m-1}, \Sigma_0)$ where $\xi_1 \sim N(0, \Sigma_0)$, $D = \text{diag}(0.99, \dots, 0.99) \in \mathbb{R}^{L \times L}$, and $\Sigma_0 \in \mathbb{R}^{L \times L}$ is a covariance matrix that varies by scenario. In Scenario A, we simulate genomic covariates as independent by setting $\Sigma_0 = I_L$; in Scenario B, we make them correlated by sampling Σ_0 using the function `genPositiveDefMat` with `covMethod = "onion"` from the R package `clusterGeneration`; refer to [Joe \(2006\)](#). We then set $\mathbf{x}(t) = (\mathbf{z}_m - \bar{\mathbf{z}})/\text{sd}(\mathbf{z})$ for $t \in [\tau_m, \tau_{m+1})$, where $\bar{\mathbf{z}} = \frac{1}{M} \sum_{m=1}^M \mathbf{z}_m$, the scaling $\text{sd}(\mathbf{z}) = \left(\frac{1}{M-1} \sum_{m=1}^M (\mathbf{z}_m - \bar{\mathbf{z}})^2 \right)^{1/2}$ is computed coordinate-wise, and “/” denotes coordinate-wise division. Hence, our synthetic genome comprises $M = 2000$ regions and has piecewise constant covariates with mean zero and variance one.

Copy numbers. For each patient j , we generate the copy numbers $c_j(t)$ as follows. Draw $S_j \sim \text{Poisson}(20)$ and split $[0, T)$ into S_j contiguous segments by randomly selecting segment boundaries uniformly without replacement from $\{\tau_1, \dots, \tau_M\}$. For each segment $s = 1, \dots, S_j$, we sample $V_{js} \sim \text{NegBin}(1, 10)$ independently, where $\text{NegBin}(m, v)$ denotes the negative binomial with mean m and variance $m(1 + m/v)$. We then set $c_j(t) = V_{js} + 2$ for all positions t in segment s .

Model parameters. We define the true signature matrix $R_0 \in \mathbb{R}^{I \times K_0}$ with $I = 96$ by setting the first four columns equal to the COSMIC signatures frequently appearing in breast cancer, namely SBS1, SBS2, SBS13, and SBS3; see Section 5 for their interpretation. The remaining $K_0 - 4$ columns are sampled as $r_k^0 \sim \text{Dir}(0.1, \dots, 0.1)$

independently. We generate the true baseline activities $\Phi_0 \in \mathbb{R}^{K \times J}$ as $\phi_{kj}^0 = \mu_k^0 \nu_{kj}^0 / \int_0^T \frac{1}{2} c_j(t) dt$, with $\mu_k^0 \sim \text{Ga}(100, 1)$ and $\nu_{kj}^0 \sim \text{Ga}(0.5, 0.5)$ independently. We simulate the true coefficients by sampling $\beta_k^0 \sim \text{N}(\mathbf{0}, \sigma_0^2 I_L)$, with $\sigma_0^2 = 1/2$, and we define $B_0 \in \mathbb{R}^{K \times L}$ as the matrix with columns β_k^0 .

Mutations. For each $i = 1, \dots, I$ and $J = 1, \dots, J$, we simulate mutations along $[0, T]$ by sampling from a Poisson process using the inverse cumulative intensity function. First, we sample the total number of mutations as $N_{ij} \sim \text{Poisson}(\Lambda_{ij})$, where $\Lambda_{ij} = \int_0^T \lambda_{ij}(t) dt = \sum_{m=1}^M (\tau_{m+1} - \tau_m) \lambda_{ij,m}$, and $\lambda_{ij,m} = \sum_{k=1}^K r_{ik}^0 \phi_{kj}^0 \frac{1}{2} c_{jm} e^{\beta_k^{0\top} \mathbf{x}_m}$ with c_{jm} and \mathbf{x}_m denoting the values of the copy number and the covariates in bin m . Then, we sample $U_n \sim \text{U}(0, \Lambda_{ij})$ for $n = 1, \dots, N_{ij}$ independently, and for each n , we find the bin index m_n for which $\sum_{m=1}^{m_n} \lambda_{ij,m} \leq U_n < \sum_{m=1}^{m_n+1} \lambda_{ij,m}$. Finally, $t_{ijn} \sim \text{U}(\tau_{m_n}, \tau_{m_n+1})$.

S4.2 FURTHER SIMULATION RESULTS

We present an extended version of the simulation results in Section 4, using the following methods. All the models considered are variants of PPF except the CompNMF model, although this can also be viewed as a special case of PPF.

- M0) MAP, true \mathbf{x} : the MAP with only the $L = 5$ covariates used to generate the data, and with $c_j(t)$ set to the true values.
- M1) MAP, CompNMF: the MAP of the Poisson NMF model in Equation (1) with prior as in Zito and Miller (2024). (No covariates, no copy numbers.)
- M2) MAP, no \mathbf{x} : the MAP with no covariates, and with $c_j(t)$ set to the true copy numbers.
- M3) MAP, all \mathbf{x} : the MAP with all $L = 10$ covariates, and with $c_j(t)$ set to the true copy numbers.
- M4) MCMC, all \mathbf{x} : the posterior mean for the same model as M3, calculated by starting Algorithm 2 from the MAP.
- M5) MCMC, all \mathbf{x} , $\Delta_b = 200$: same as M4, but with covariates aggregated by further averaging their values over groups of two consecutive of bins.
- M6) MCMC, all \mathbf{x} , $\Delta_b = 500$: same as M5, but averaging over groups of 5 consecutive bins.

We use the default PPF model settings in Section 2.4 for a , α_{ik} , ε , c_0 , and d_0 , and we set $K = 15$ for the upper bound on the number of signatures. Our goal is to compare the performance of different versions of model and algorithm, in order to assess the utility of various aspects. For example, comparing M3 to M0 quantifies any loss in performance due to including irrelevant covariates. Meanwhile, comparing M5 to M4 evaluates whether there is a loss in performance due to approximating the integral in Equation (10) using a coarser grid than the true data-generating process.

Estimation performance. Figure S1 shows the results for both scenarios: (A) independent covariates, (B) correlated covariates. In addition to the quantities displayed in Figure 2, we also show a panel reporting the estimated number of signatures \hat{K} in each replicate, and a panel reporting the F_1 score for each replicate. The F_1 score is defined as $F_1 = 2 \times \text{precision} \times \text{sensitivity} / (\text{precision} + \text{sensitivity})$, where *precision* is the proportion of estimated signatures that have a cosine similarity ≥ 0.9 with at least one of the ground truth signatures, and *sensitivity* is the proportion of ground truth signatures for which there is an estimated signature with cosine similarity ≥ 0.9 (Islam et al., 2022). Hence, F_1 is a measure of how similar \hat{R} and R_0 are, with values close to 1

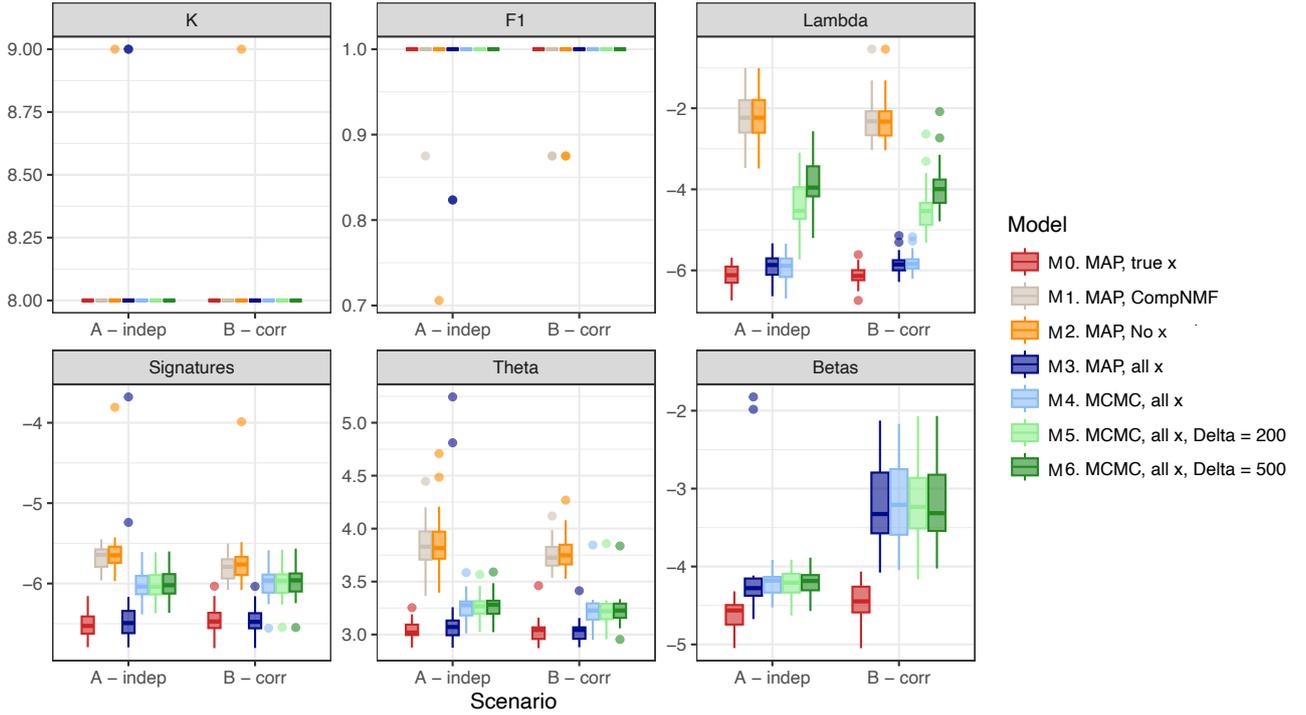


Figure S1: Extended simulation results. The panel titled “K” shows the estimated number of signatures across the 20 replicates. Panel “F1” shows the F_1 score. The remaining panels report the $\log(\text{RMSE})$ for the same quantities as in Figure 2.

indicating high similarity. The other panels display the $\log(\text{RMSE})$ with respect to the true quantities, where the logarithm is taken to aid visualization.

Several points are worth noting in these results.

- **Benefit of covariates.** PPF with covariates (e.g., M0 and M3) provides a major improvement in performance compared to the baseline NMF model (M1), in terms of the estimated total intensity Λ , signatures R , and total activity Φ . In contrast, using copy numbers without covariates (M2) provides little to no benefit over the baseline NMF model (M1).
- **Recovery of K .** On these data, all versions accurately recover the true number of factors ($K = 8$) and have a perfect F_1 score with only a few exceptions. Thus, any differences in performance are not due to incorrect recovery of K .
- **Impact of extra covariates.** As expected, including unneeded covariates (M3) can reduce performance relative to including only the covariates used to generate the data (M0), particularly in Scenario B (correlated covariates). While this loss in performance is substantial for estimating the coefficients B , there is little difference in performance for estimating Λ , R , and particularly Φ , for which there is essentially no difference.
- **MCMC versus MAP.** Curiously, the MAP estimate (M3) tends to be more accurate than the posterior mean from MCMC (M4) in terms of the signatures R and total activity Θ . This is a natural consequence of the optimization algorithm.

- **Resolution of covariate aggregation.** Using a coarser scale of aggregation for the covariates (M5 and M6) has little impact on estimation of the signatures R , total activity Φ , and coefficients B , compared to using a finer scale (M4). However, it does reduce the accuracy of the total intensity Λ .
- **Impact of correlated covariates.** For all methods, performance in Scenario B is comparable to Scenario A for estimating K , Λ , R , and Φ . However, estimation of B is noticeably worse in Scenario B, particularly when irrelevant covariates are included.

Overall, the best performance is obtained when using PPF with the MAP estimate, including covariates and copy numbers.

Computation time. We further benchmark the performance in terms of computation time and number of iterations to run each method. Table S1 shows the wall clock time for the MAP-based methods. The PPF models (M0, M2, and M3) do take considerably longer than the baseline NMF model (M1), however, requiring only 20-30 minutes to fit such a flexible model is quite reasonable. As expected, including more covariates requires more time, as we go from $L = 0$ (M2) to $L = 5$ (M0) to $L = 10$ (M3) covariates. For all MAP methods, the computational burden is comparable for Scenarios A (independent covariates) and B (correlated covariates).

Table S1: Computation time and number of iterations for MAP-based methods. Shown are averages across 20 randomly generated datasets, with standard deviation in parentheses beneath each entry.

METHOD		SCENARIO A		SCENARIO B	
		TIME (MIN)	ITERATIONS	TIME (MIN)	ITERATIONS
M0)	MAP, true \mathbf{x}	23.4 (11.6)	384.5 (142.4)	23.3 (19.9)	430.5 (271.2)
M1)	MAP, CompNMF	0.009 (0.007)	4641.9 (1895.7)	0.009 (0.005)	3694.9 (1288.9)
M2)	MAP, no \mathbf{x}	8.7 (6.3)	626.0 (272.7)	7.7 (5.3)	581.0 (258.3)
M3)	MAP, all \mathbf{x}	26.8 (17.8)	373.0 (195.4)	19.8 (10.5)	343.5 (271.1)

For the MCMC algorithm, Table S2 shows the total computation time and effective sample sizes for R , Φ , B , μ , σ^2 , and the log-posterior density at the sampled parameters, for M4, M5, and M6. ESS is calculated using the samples from the last 1500 MCMC iterations, and computation time is based on all 3000 iterations. Scenarios A (independent covariates) and B (correlated covariates) are comparable in terms of MCMC computation time and ESS, except that Scenario B has lower ESS for the coefficients B , presumably since correlated covariates leads to posterior correlation between entries of B .

Table S2: Computation time and effective sample sizes (ESS) for MCMC. Shown are averages across 20 datasets, with standard deviations in parentheses. ESS is calculated over 1500 samples.

METHOD	TIME (MIN)		ESS R		ESS Θ		ESS B		ESS μ		ESS σ^2		ESS logPost	
	A	B	A	B	A	B	A	B	A	B	A	B	A	B
M4) MCMC, all \mathbf{x} , $\Delta_b = 100$	132 (29)	137 (32)	388 (43)	389 (36)	439 (41)	454 (39)	49 (2)	19 (3)	1172 (128)	1206 (123)	1433 (57)	1312 (103)	467 (62)	474 (78)
M5) MCMC, all \mathbf{x} , $\Delta_b = 200$	142 (18)	141 (19)	388 (42)	389 (36)	444 (37)	453 (38)	49 (2)	19 (4)	1167 (103)	1216 (94)	1463 (57)	1334 (77)	485 (97)	491 (62)
M6) MCMC, all \mathbf{x} , $\Delta_b = 500$	92 (18)	93 (27)	385 (42)	386 (35)	441 (38)	455 (38)	48 (2)	19 (3)	1182 (109)	1218 (118)	1452 (60)	1294 (112)	489 (68)	463 (105)

S5 ADDITIONAL DETAILS ON BREAST CANCER APPLICATION

S5.1 DATA SOURCES

Mutation data for the breast cancer cohort can be downloaded from https://pcawg-hub.s3.us-east-1.amazonaws.com/download/October_2016_whitelist_2583.snv_mnv_indel.maf.xena.nonUS. Copy number data for the same cohort of patients can be downloaded from https://pcawg-hub.s3.us-east-1.amazonaws.com/download/20170119_final_consensus_copynumber_donor.

Table S3: Summary of ENCODE and GEO sources used to assemble covariate data.

Repository	Covariate	Measurement	Type	File
ENCODE	CTCF	Fold change over control	Primary cell	ENCFF101RHP.bigWig
ENCODE	H3K27ac	Fold change over control	Primary cell	ENCFF981WTU.bigWig
ENCODE	H3K27me3	Fold change over control	Primary cell	ENCFF322JKF.bigWig
ENCODE	H3K36me3	Fold change over control	Primary cell	ENCFF175PNA.bigWig
ENCODE	H3K4me1	Fold change over control	Primary cell	ENCFF531OEA.bigWig
ENCODE	H3K4me3	Fold change over control	Primary cell	ENCFF094MQS.bigWig
ENCODE	H3K4me3	Fold change over control	Primary cell	ENCFF240TPI.bigWig
ENCODE	H3K4me3	Fold change over control	Primary cell	ENCFF925FUX.bigWig
ENCODE	H3K9me3	Fold change over control	Primary cell	ENCFF709GNN.bigWig
ENCODE	CTCF	Fold change over control	Tissue	ENCFF143AFG.bigWig
ENCODE	CTCF	Fold change over control	Tissue	ENCFF663JVM.bigWig
ENCODE	H3K27ac	Fold change over control	Tissue	ENCFF984VUL.bigWig
ENCODE	H3K27me3	Fold change over control	Tissue	ENCFF353WUO.bigWig
ENCODE	H3K36me3	Fold change over control	Tissue	ENCFF529OVO.bigWig
ENCODE	H3K4me1	Fold change over control	Tissue	ENCFF467DBD.bigWig
ENCODE	H3K4me3	Fold change over control	Tissue	ENCFF216DKX.bigWig
ENCODE	H3K9me3	Fold change over control	Tissue	ENCFF764JHZ.bigWig
ENCODE	Nucleosome occupancy	Signal	K562	GSM920557_hg19_wgEncodeSydhNsomeK562Sig.bigWig
ENCODE	Replication timing	Wavelet-smoothed signal	MCF7	wgEncodeUwRepliSeqMcf7WaveSignalRep1.bigWig
BSgenome	GC content	Percent	hg19	BSgenome.Hsapiens.UCSC.hg19
GEO	Methylation	Beta score		GSM5652347_Breast-Luminal-Epithelial-Z000000V2.bigwig
GEO	Methylation	Beta score		GSM5652348_Breast-Luminal-Epithelial-Z000000VJ.bigwig
GEO	Methylation	Beta score		GSM5652349_Breast-Luminal-Epithelial-Z000000VN.bigwig
GEO	Methylation	Beta score		GSM5652350_Breast-Basal-Epithelial-Z000000V6.bigwig
GEO	Methylation	Beta score		GSM5652351_Breast-Basal-Epithelial-Z000000VG.bigwig
GEO	Methylation	Beta score		GSM5652352_Breast-Basal-Epithelial-Z000000VL.bigwig
GEO	Methylation	Beta score		GSM5652353_Breast-Basal-Epithelial-Z00000043E.bigwig

S5.2 DATA PREPROCESSING

We assembled the covariate data in Table 1 from various sources; see Table S3. Specifically, we consider a set of data similar to the one previously analyzed by [Otlu et al. \(2023\)](#), whose goal is to study the relationship between epigenetic markers and mutational signatures. We downloaded from ENCODE all the `bigWig` files associated with the `bed` files indicated in the supplement of [Otlu et al. \(2023\)](#). While `bed` files report the regions having statistically significant enrichments from a covariate, `bigWig` formats contain the signal for the whole genome; hence, they are better suited for our application. We use the files that measure the fold-change over control from the ChIP-seq assay for both histone modifications and CTCF binding. This unit of measurement has a more transparent interpretation as opposed to $-\log_{10}$ p-values, which is instead used for visualization purposes and to identify significant peaks. Replication timing is obtained from data on the MCF-7 breast cancer cell line, as in [Morganella et al. \(2016\)](#). As for nucleosome occupancy, we use data from an MNase-seq assay on the K562 leukemia cell line ([Tolstorukov et al., 2011](#)). Despite not being breast-specific, it is one of the few

datasets on nucleosome position that is derived from cancer cells (Otlu et al., 2023). Finally, methylation data are obtained from Loyfer et al. (2023) and migrated from genome hg38 to hg19 using `liftOver`.

Our pre-processing steps are the following. We subdivide chromosomes 1 to 22 and X in the hg19 reference genome into non-overlapping regions of 2,000 nucleotides (2kb aggregation) via the `tileGenome` function in the R package `GenomicRanges` (Lawrence et al., 2013). Chromosome Y is excluded because all patients are female. We assign to each bin a weight Δ_m , calculated as the number of nucleotides in a region, excluding the portions that overlap with any of the problematic regions listed by Amemiya et al. (2019). Hence, if a region is not problematic and does not have any missing values “N”, we have $\Delta_m = 2,000$. Meanwhile, $\Delta_m = 0$ implies that no mutation can be detected in that bin. We subdivide the copy number data for each patient using the same partition, and call c_{jm} the number of copies for patient j in bin m . As for the covariates, we first import into memory each `bigWig` file in Table S3 using the `rtracklayer` package (Lawrence et al., 2009) and then calculate the average value of the signal in every bin using the function `binnedAverage` in `GenomicRanges`. Signals from different files representing the same covariate are then averaged in each bin. As for GC content, we simply calculate the fraction of G or C nucleotides in the 2kb bins via the function `letterFrequency` in the package `Biostrings` (Pagès et al., 2023). This results in 11 piecewise constant covariates aligned to the same coordinates, with a total of $M = 1,391,345$ bins having a non-zero weight $\Delta_m > 0$ and with $T = \sum_{m=1}^M \Delta_m = 2,780,909,076$. This is lower than the overall length of hg19 due to the presence of blacklisted regions. Finally, we cap the value of all covariates at their 99.9th percentile to avoid excessively long tails, and we standardize them to have a mean of zero and a variance of one across bins $m = 1, \dots, M$.

The covariates in this analysis are not patient-specific, but instead correspond to a reference epigenome that is common to all patients. Moreover, except for nucleosome occupancy and replication timing, all assays are run on tissues and cell lines from breast epithelium obtained from a separate group of healthy donors. Hence, our analysis detects associations that reflect mutational biases in the cancer genomes that are not driven by patient-specific alterations in the chromatin. The 2kb scale is motivated by the need to balance between information at the original `bigWigs` resolution, and computational feasibility when running estimation algorithms. In particular, when $A = [0, T)$, the integral in Equation (5) is equal to

$$\int_0^T \frac{1}{2} c_j(t) e^{\beta_k^\top \mathbf{x}(t)} dt = \sum_{m=1}^M \Delta_m \frac{1}{2} c_{jm} e^{\beta_k^\top \mathbf{x}_m},$$

where \mathbf{x}_m and c_{jm} denote the constant values of the covariates and the copy numbers in each bin. Using finer partitions leads to heavier computational and memory requirements, while coarser partitions may obscure the effect of covariates operating at smaller scales, such as CTCF. Furthermore, a 2kb window size centered at each mutation (± 1000 bases) is the proposed size in the analyses of Otlu et al. (2023) when analyzing mutational signatures contributions near histone modification and transcription factors.

S5.3 FURTHER RESULTS

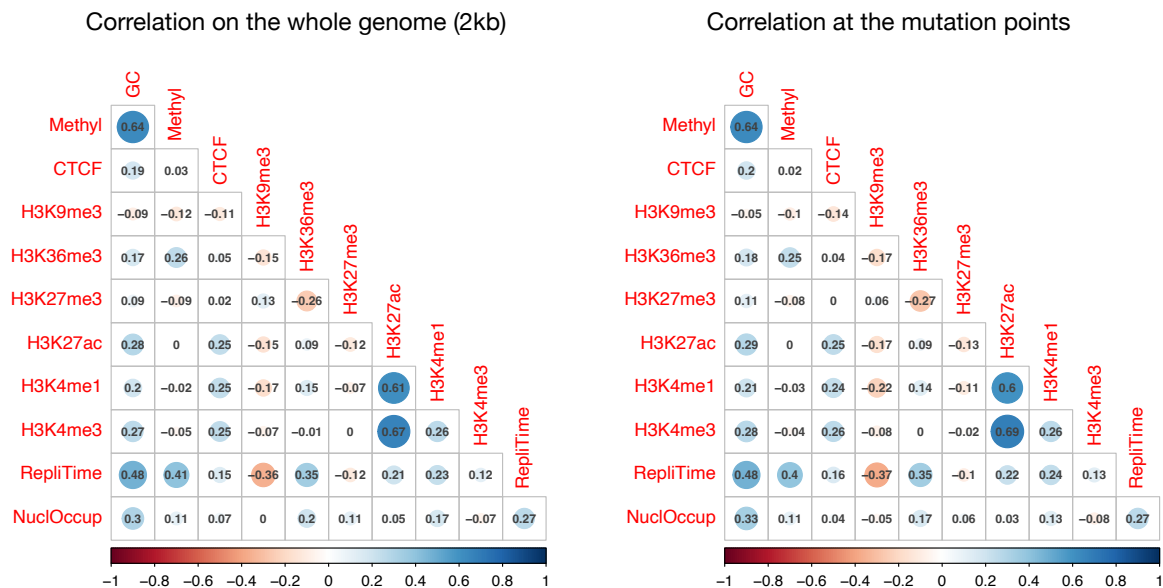


Figure S2: Correlation between genomic covariates at the 2kb resolution. Left: correlations over the whole genome. Right: correlation of the values at the mutation points. Regions that have $\Delta_m = 0$ have been excluded to compute the values.

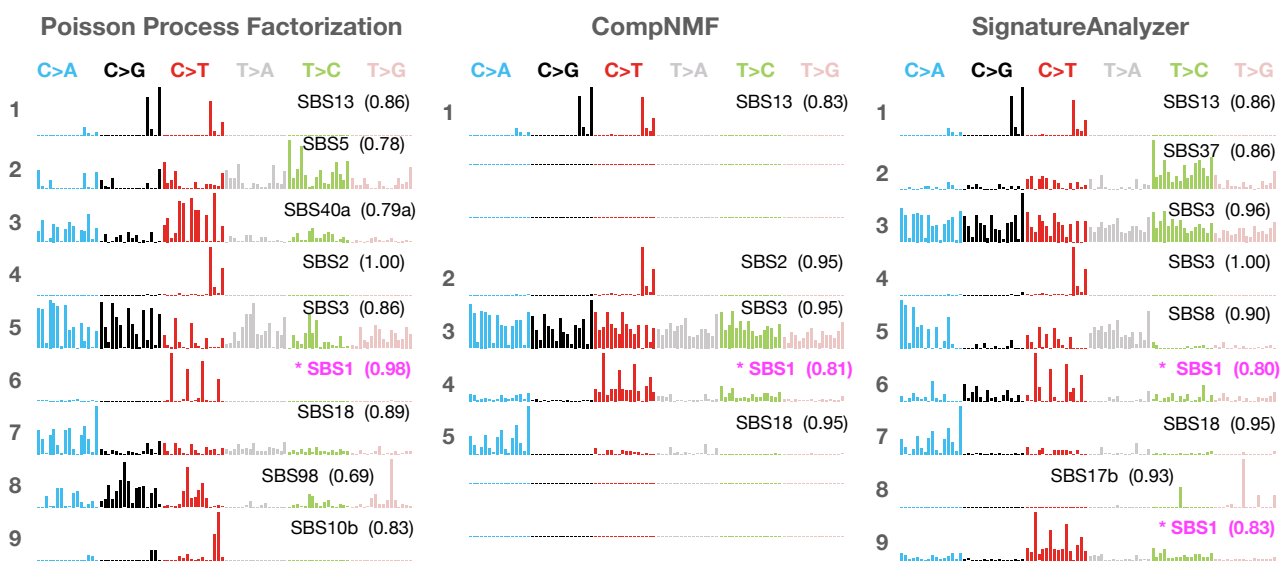


Figure S3: Estimated signatures in ICGC breast adenocarcinoma. Left: results from Poisson process factorization. Center: results from baseline Poisson NMF (CompNMF) using Algorithm S1. Right: results from SIGNATUREANALYZER. We highlight SBS1 with an asterisk in magenta, to highlight the similarities and ensure a better comparison.

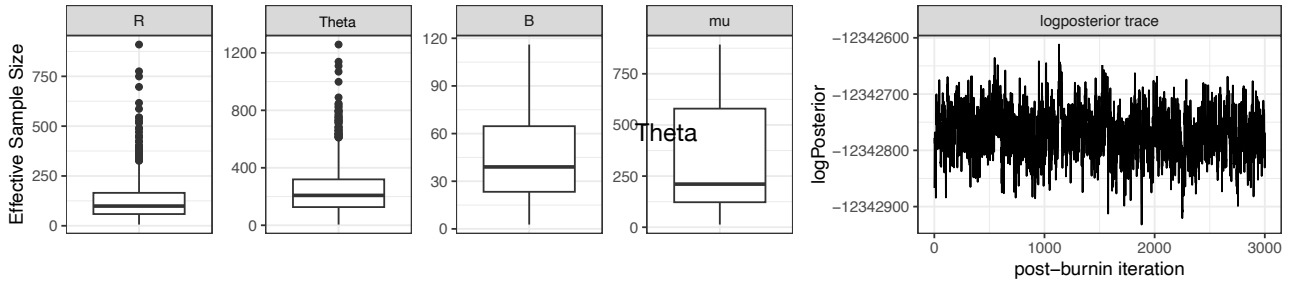


Figure S4: Left: effective sample sizes for model parameters in the *de novo* analysis. Right: traceplot for the log posterior density. Values are computed over 3,000 iterations after burn-in.

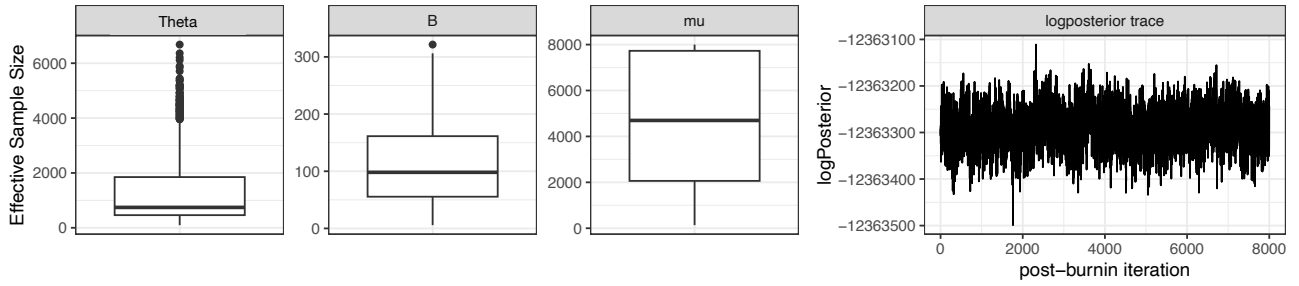


Figure S5: Left: effective sample sizes for model parameters in the fixed-signatures analysis. Right: traceplot for the log posterior. Values are computed over 8,000 iterations after burn-in.